

We are IntechOpen, the world's leading publisher of Open Access books Built by scientists, for scientists

6,900

Open access books available

185,000

International authors and editors

200M

Downloads

Our authors are among the

154

Countries delivered to

TOP 1%

most cited scientists

12.2%

Contributors from top 500 universities



WEB OF SCIENCE™

Selection of our books indexed in the Book Citation Index
in Web of Science™ Core Collection (BKCI)

Interested in publishing with us?
Contact book.department@intechopen.com

Numbers displayed above are based on latest data collected.
For more information visit www.intechopen.com



Fractal Antennas for Wireless Communications

Amer T. Abed, Mahmood J. Abu-AlShaer and Aqeel M. Jawad

Abstract

When the length of the antenna is less than a quarter of the wavelength of the operating frequency, good radiation properties are difficult to obtain. However, size limitations can be overcome in this case using a fractal geometry antenna. The shape is repeated in a limited size such that the total length of the antenna is increased to match, for example, half of the wavelength of the corresponding desired frequency. Many fractal geometries, e.g., the tree, Koch, Minkowski, and Hilbert fractals, are available. This chapter describes the details of designing, simulations, and experimental measurements of fractal antennas. Based on dimensional geometry in terms of desired frequency bands, the characteristics of each iteration are studied carefully to improve the process of designing the antennas. In depth, the surface current distribution is investigated and analyzed to enhance the circular polarization radiation and axial ratio bandwidth (ARBW). Both, simulation and experimental, results are discussed and compared. Two types of fractal antennas are proposed. The first proposed fractal antenna has a new structure configured via a five-stage process. The second proposed fractal antenna has a low profile, wherein the configuration of the antenna was based on three iterations.

Keywords: fractal antenna, compact size, circular polarization

1. Introduction

Fractal means broken or irregularly fragmented and refers to a family of complex shapes that possess an inherent self-similarity in their geometrical structures. Good radiation properties are difficult to obtain when the length of the antenna is less than a quarter of the wavelength for the operating frequency. However, size limitations can be overcome in this case using a fractal geometry antenna. The shape is repeated in a limited size such that the total length of the antenna is increased to match, for example, half of the wavelength of the corresponding desired frequency. Many fractal geometries, such as tree, Koch, Minkowski, and Hilbert fractals, are used in designing antennas [1]. But through using a fractal geometry antenna, where the shape is repeated in a limited size, in a way that increases the total length of the antenna to match, for example, half of the wavelength of the corresponding desired frequency, the size limitations can be overcome in this case. Many fractal geometries such as the tree, Koch, Minkowski, and Hilbert fractals are used in designing this type of antenna.

There are many geometries used in designing fractal antennas such as: Fractal slot [2], Giuseppe Peano Fractal Geometries [3], Fractal loop [4], Fractal Cantor [5],

Minkowski Fractal [6], Koch Fractal [7], H-Fractal [8], Sierpinski gasket arrangement [9], Fern Fractal leaf [10], Mandelbrot Fractal antenna [11], Amer fractal slot [12], Sunflower Fractal [13], Flame Fractal [14] and Butterfly Structure [15].

2. Compact fractal antenna

One of the most widely used structures in fractal antennas is Sierpinski gasket [16]; it consists of equilateral triangles. There are two ways to build this structure, either by the decomposition method or by a multiple copy method. In this research, the second method is used in designing the fractal antenna; **Figure 1** represents this method.

At the first iteration, the structure made two copies of the same triangle in the 0th iteration, one of them located on its side while the other located above them. In the second iteration the same process is repeated, but with all first iteration structure. So the dimensions of the next iteration increased by factor 3 compared with the dimensions of the previous iteration. The above transformation of the triangle to generate any order of iterations can be represented by the mathematical formula [16]:

$$W \begin{bmatrix} x \\ y \end{bmatrix} = \begin{bmatrix} r \cos \theta & -s \cos \varnothing \\ r \sin \theta & s \sin \varnothing \end{bmatrix} \begin{bmatrix} x \\ y \end{bmatrix} + \begin{bmatrix} x_0 \\ y_0 \end{bmatrix} \quad (1)$$

where r and s are the scale factor, θ and \varnothing are the rotation angles, and x_0 and y_0 are the amounts of translation. If the factors r, s are either reductions or magnifications, the transformation process is called self-affine, while, if $r = s$ and $\theta = \varnothing$, the transformation is called self-similar.

The structure of the proposed antenna is new; the initiator is a square patch as shown in **Figure 2a**; the two arms of the patch are equal and unity, i.e., $x = y = 1$. In 0th iteration, four symmetrical slots are cut in the square patch as shown in **Figure 2b**. The modified patch (**Figure 2c**) is configured by cutting increasable slips to change the dimensions of the arms at the corners in a way to configure asymmetrical corner dimensions:

$$W \begin{bmatrix} x \\ y \end{bmatrix} = \begin{bmatrix} r \cos \theta & -s \cos \varnothing \\ r \sin \theta & s \sin \varnothing \end{bmatrix} \begin{bmatrix} x \\ y \end{bmatrix} + \begin{bmatrix} x_0 \\ y_0 \end{bmatrix} \quad (2)$$

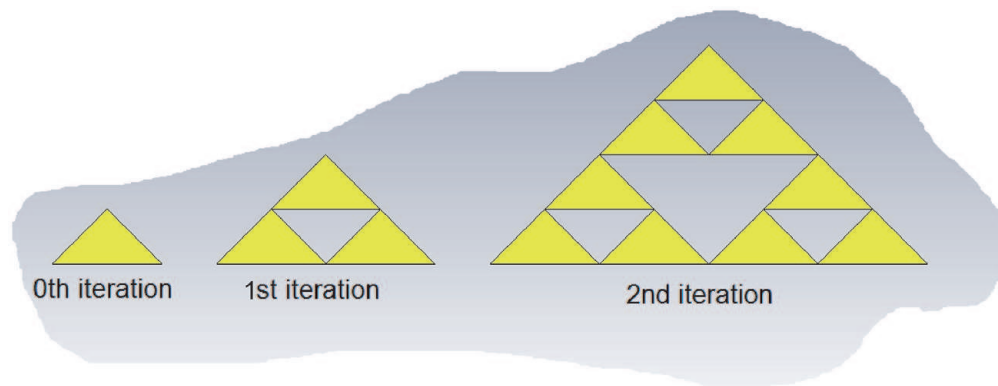


Figure 1.
Multiple copy approach of Sierpinski gasket arrangement.

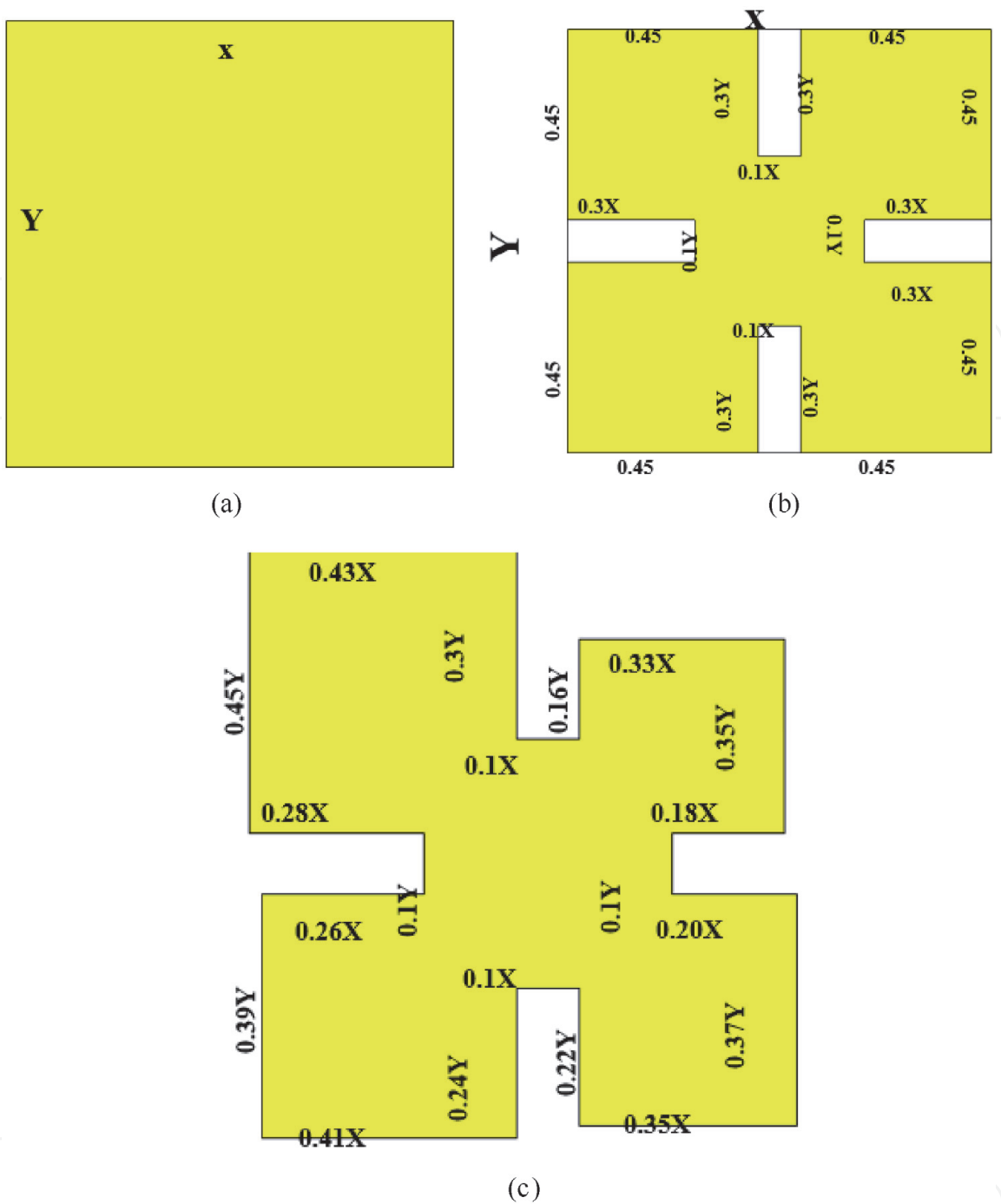


Figure 2. Configuration of fractal antenna. (a) Initiator patch. (b) 1st iteration. (c) Modified patch.

The upper arm in **Figure 2c** has total length $0.43x + 0.3y + 0.1x + 0.16y + 0.33x = 1.32x$, where $x = y$. The left arm's length is $0.45y + 0.28x + 0.1y + 0.26x + 0.39y = 1.48x$. The lower arm length is $0.41x + 0.24y + 0.22y + 0.1x + 0.35x = 1.32x$. The right arm length is $0.37y + 0.2x + 0.1y + 0.18x + 0.35y = 1.2x$. So, each arm in the square patch (**Figure 2a**) has unity length ($x = y$), while the lengths of the arms in the modified patch expand to $1.32x$, $1.48x$, and $1.2x$. This expedition gives two additional properties in designing the fractal antenna.

Firstly, different electrical lengths of the arms generate many resonant frequencies which can be integrated to have wide operating bands.

Secondly, different lengths of both sides of each corner, for example, the lengths of the two sides of the right-upper corner, are $0.35y$ and $0.33x$; this difference in lengths is useful to generate two orthogonal modes with phase shift 90° which are

very important requirements to create circularly polarized radiation. The modified patches will be arranged in a cascade arrangement to increase the total electrical length of the antenna to generate resonant frequencies have wave lengths \gg of the physical length of the antenna. **Figure 4** represents the arrangement of the cascade modified patch (two symmetrical structures). According to Eq. (1), the affine transformations will be:

$$W_2 \begin{bmatrix} x \\ y \end{bmatrix} = \begin{bmatrix} 0.25 & 0.25 \\ 0 & 0 \end{bmatrix} \begin{bmatrix} x \\ y \end{bmatrix} + \begin{bmatrix} 0 \\ 6.375 \end{bmatrix} \quad (3)$$

If the x -axis is the bottom of the left modified patch and y -axis passes through the center of the left modified patch in **Figure 3**, W_1 configures by adding a half size of the modified patch in **Figure 3** to both structures (left and right sides). The dotted yellow line in **Figure 3** is on the y -axis and passes through all centers (black points) of the transformation structures (W_1, W_2 and W_3), so the scale factors are ($r = s = 0.5$), the rotation angles are $\theta = \phi = 0$, and the translation factors are ($x_0 = 0, y_0 = 4.25$):

$$W_1 \begin{bmatrix} x \\ y \end{bmatrix} = \begin{bmatrix} 0.5 & 0.5 \\ 0 & 0 \end{bmatrix} \begin{bmatrix} x \\ y \end{bmatrix} + \begin{bmatrix} 0 \\ 4.25 \end{bmatrix} \quad (4)$$

While W_2 is done by adding quarter size of the modified patch, the scale factors are ($r = s = 0.25$), there are no rotation angles, and the translation factors are ($x_0 = 0, y_0 = 6.375$):

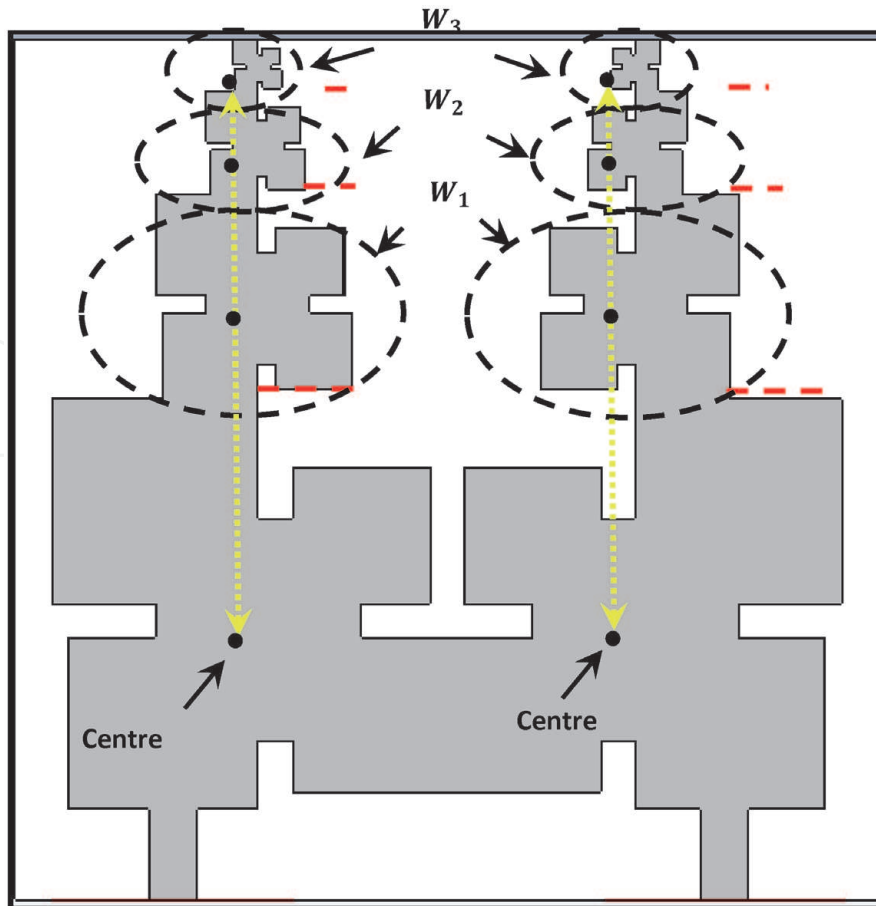


Figure 3.
Fractal dual-input antenna.

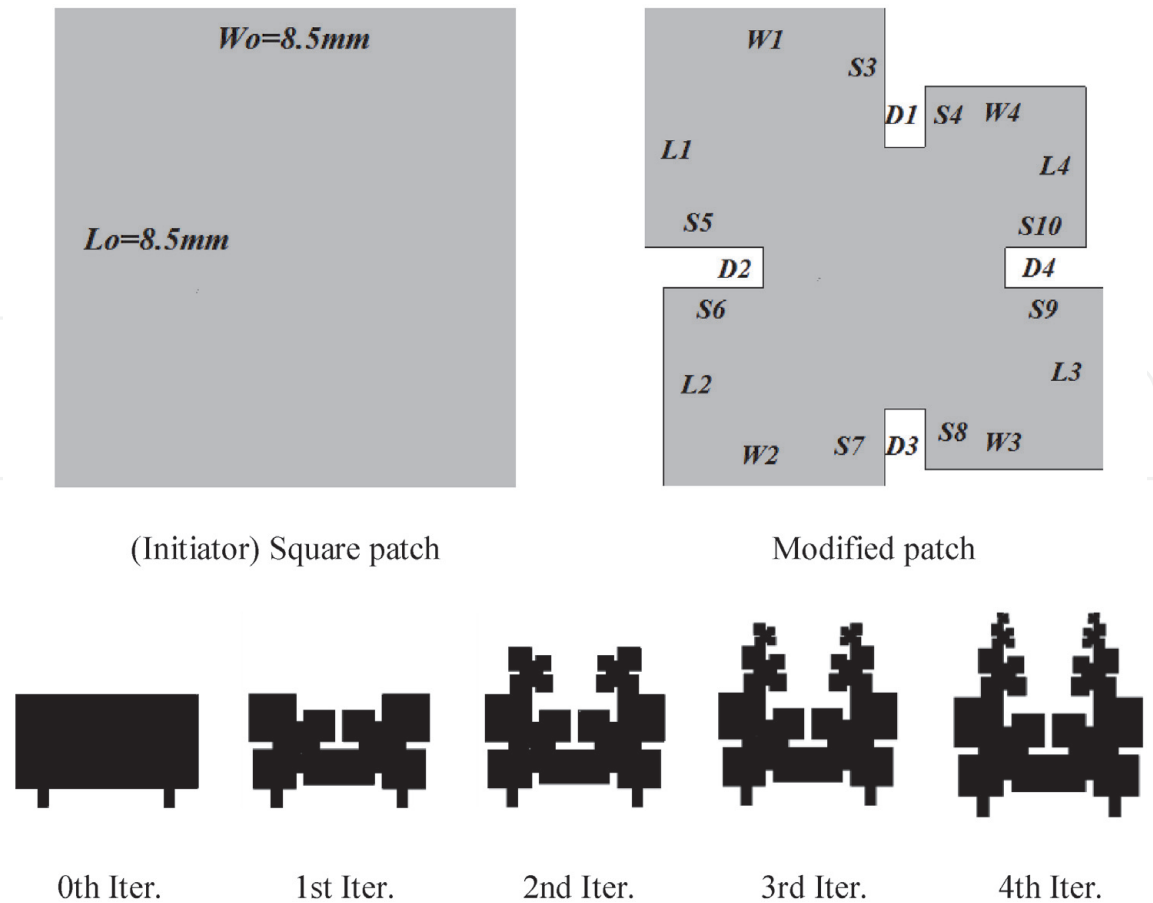


Figure 4.
Process of fractal antenna configuration.

$$W_2 \begin{bmatrix} x \\ y \end{bmatrix} = \begin{bmatrix} 0.25 & 0.25 \\ 0 & 0 \end{bmatrix} \begin{bmatrix} x \\ y \end{bmatrix} + \begin{bmatrix} 0 \\ 6.375 \end{bmatrix} \quad (5)$$

And for W_3 , the scale factors are ($r = s = 0.1250$) and the translation factors are ($x_0 = 0, y_0 = 7.4375$):

$$W_3 \begin{bmatrix} x \\ y \end{bmatrix} = \begin{bmatrix} 0.125 & 0.125 \\ 0 & 0 \end{bmatrix} \begin{bmatrix} x \\ y \end{bmatrix} + \begin{bmatrix} 0 \\ 7.4375 \end{bmatrix} \quad (6)$$

The antenna had dual operating bands that meet the specifications of the Wi-Fi and WiMAX applications. The structure of the antenna was carefully studied and analyzed so as to achieve a diversity of circular polarization (RHCP and LHCP) by switching the inputs.

The proposed antenna consisted of two symmetrical fractal structures as shown in **Figure 4**. The radiated plate is etched on a FR-4 substrate with $\epsilon_r = 4.3$, $\tan \delta = 0.027$, and compact size of $18 \times 18 \times 0.8 \text{ mm}^3$, while the dimensions of the ground plate are $18 \text{ mm} \times 14.5 \text{ mm}$. **Figure 4** shows the initiator; it is a square patch with dimensions of ($L_o = W_o = 8.5 \text{ mm}$). The square patch is modified by cutting equal slots ($0.1L_o = 0.1W_o$) in the middle of each arm and then modifying the dimensions of the arms at the corners by cutting increasable slips to change the dimensions of the arms at the corners in a way to configure asymmetrical corners, so the dimensions of each corner are not matching the others to generate different resonant frequencies that collected together to have wide impedance bandwidth. This

modified square patch looks like the logo of Microsoft Office; it is the basic structure for the construction of the proposed antenna. All dimensions are illustrated in **Table 1**.

Figure 4 shows that antenna 0 (0th iteration) is made through the integration of two square patches. The first iteration consists of dual modified square patches, while the second iteration is made by adding a half size of the modified patch to the first iteration. The same procedure is to be applied to the third iteration, except for the fact that the additional modified patch has quarter size of the original one and antenna 4 (the fourth iteration) is configured by adding $\frac{1}{8}$ of the size of the original modified square patch to antenna 3. In this way, the modified patches are arranged in cascade arrangement so as to increase the total electrical length of the antenna of the same size. **Figure 4** represents the arrangement of the cascade modified patch (two symmetrical structures). According to Eq. (1), W_1 configures by adding a half size of the modified patch in **Figure 4** to both structures (left and right sides). The dotted yellow line in **Figure 5** is in the Y-axis and passes through all centers (black points) of the transformation structures (W_1 , W_2 and W_3) which are calculated previously.

From Eq. (4), for the transformed function W_1 , the scale factors are $r = s = 0.5$, the rotation angles $\theta = \varnothing = 0$, and the translation factors ($x_0 = 0, y_0 = 4.25$). Eq. (5) represents the values of scale factor ($r = s = 0.25$), the values of the rotation angle (0), and values of scale factor ($x_0 = 0, y_0 = 6.375$) for the transformed structure W_2 . According to Eq. (6), the values of scale factor ($r = s = 0.125$), values of the rotation angle are (0), and values of scale factor are ($x_0 = 0, y_0 = 7.4375$) for the transformed structure W_3 .

So, antenna 1 (first iteration) is formed by the integration of two modified patch antennas—each is fed by symmetrical strip lines F_1 and F_2 —the second iteration is made by adding half size of the modified patch to antenna 1 to configure antenna 2. The same procedure is applied in the third iteration except for the fact that the additional modified patch has quarter size of the original one (see **Figure 5**). Antenna 4 (fourth iteration) is configured by adding $\frac{1}{8}$ of the size of the original modified patch to antenna 3.

2.1 Resonant frequencies

The resonant frequency for the square patch antenna (the initiator) can be calculated by empirical Eq. (7), which is almost equal to ≈ 8.6 GHz. Since antenna 0 (0th iteration) is configured by the integration of twin square patches, there are two resonant frequencies, for one patch 8.5 GHz and for twin patch 4.3 GHz, which is matched with the notched resonant frequencies 4.5 GHz and 8.97 GHz observed in **Figure 6** (the dotted curve). By modifying the square patches in the first iteration

Para	mm	Para	mm	Para	mm	Para	mm	Para	mm	Para	mm
W	18	Fw1	1	L1	4.25	W4	2.9	S6	1.76	D1	0.7
L	18	Fl2	2	W2	3.9	L4	1.1	S7	1.5	D2	0.7
S1	2.9	Fw2	1	L2	3.5	S3	2.4	S8	1	D3	0.7
S2	2.9	h	0.8	W3	3.1	S4	1	S9	1.7	D4	0.7
Fl1	2	W1	4.3	L3	3.25	S5	2.1	S10	1.45		

Table 1.
Dimensions for the dual-input fractal antenna (mm).

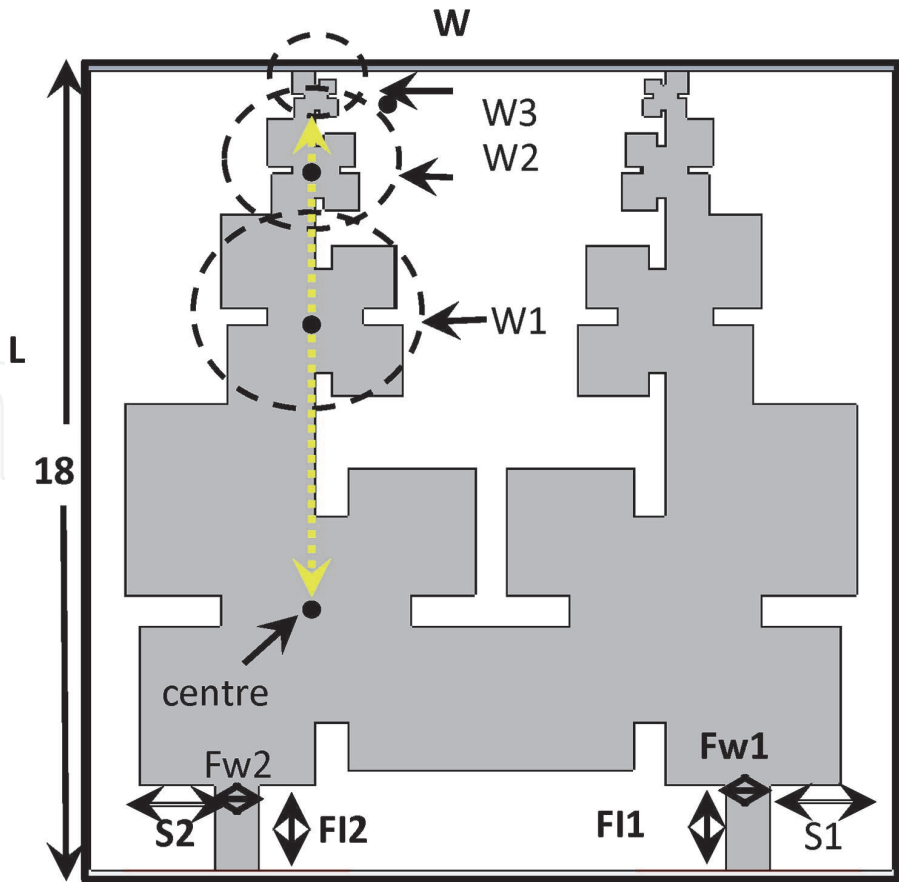


Figure 5.
The translation processes [17].

(antenna 1), the resonant frequency is shifted to 3.3 GHz, and the second band disappeared (the black curve):

$$f_r \approx \frac{c}{2L\sqrt{\epsilon_r}} \tag{7}$$

The perimeter of the modified patch (**Figure 2c**) is 42 mm, while the perimeter of the square patch (**Figure 2a**) is 34 mm, and it is well known that different dimensions create different resonant frequencies. If the perimeter of the square patch is denoted by P_0 , the perimeter of the modified patch is P_1 , and the perimeter of the first iteration is P_2 , so:

$$P_4 = \frac{1}{2}P_3 = \frac{1}{4}P_2 = \frac{1}{8}P_1 \tag{8}$$

The perimeter of the cascade modified patches PC_i at each iteration can be calculated as:

$$PC_i = \frac{1}{2}PC_{i-1} + PC_{i-1} \quad i = 1, 2, 3 \text{ and } 4 \tag{9}$$

The term $(2L)$ in Eq. (7) represents the half perimeter of the square patch, so Eq. (7) can be rewritten as:

$$f_r \approx \frac{2C}{P\sqrt{\epsilon_{ef}}} \tag{10}$$

But, $\frac{\text{the perimeter of modified Patch}}{\text{the perimeter of square Patch}} = \frac{42}{34} = 1.23$
 Eq. (10) will be:

$$f_i \approx \frac{2C}{1.23P_i\sqrt{\epsilon_{ef}}} \quad (11)$$

Let $\frac{2C}{\sqrt{\epsilon_{ef}}} = k$, and Eq. (11) will be:

$$f_i \approx \frac{k}{1.23PC_i} \quad (12)$$

According to Eq. (12), the resonant frequency of the modified patch (the first iteration) is 3.2 GHz. While the resonant frequencies for first iteration, which are presented in **Figure 6** (the black curve), are 3.3 and 7.1 GHz. However, these resonant frequencies are not useful for Wi-Fi and WiMAX applications. For second iteration, the resonant frequency calculated by Eq. (12) is 5.2 GHz and the lower resonant frequency is 2.6 GHz, which matched the lower resonant frequency shown in **Figure 6** (the blue curve). In this way, the resonant frequencies that are calculated using Eq. (12) approximately matched the values of the resonant frequencies, as presented in **Figure 6**.

Certain dual operating bands of 2.5–2.6 GHz and 5–6 GHz in the third iteration (antenna 3) are observed in the return loss curve (the red curve; **Figure 6**). The proposed antenna (fourth iteration) has a lower operating band of 2.4–2.6 GHz around resonant frequency 2.5 GHz and an upper operating band of 4.9–6 GHz around resonant frequency 5.1 GHz as shown in **Figure 6** (the dashed curve). These operating bands meet the specifications of Wi-Fi and WiMAX applications. So, the required operating bands are achieved by using novel fractal geometry at the fourth iteration in the same size of the 0th iteration.

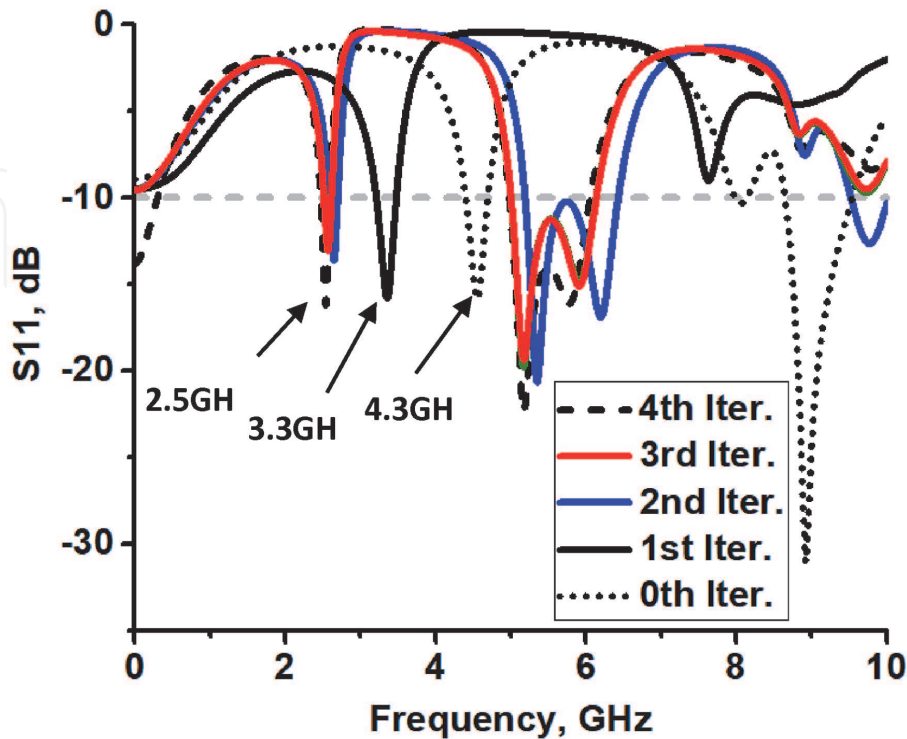


Figure 6.
 Simulated return loss values for all antennas ($S_{11} = S_{22}$) [17].

2.2 Effect of the ground size

Figure 7 shows the effect of ground size on the impedance bandwidth of the proposed fractal antenna. Given that modifying the ground dimensions can change the antenna impedance and the matching factor between the antenna and the excitation port, the dimensions of the ground plate can be modified to select the operating band.

When the dimensions of the ground plate are set to 18 mm × 10 mm, the lower operating band shifts to 3 GHz and the upper operating band disappears as

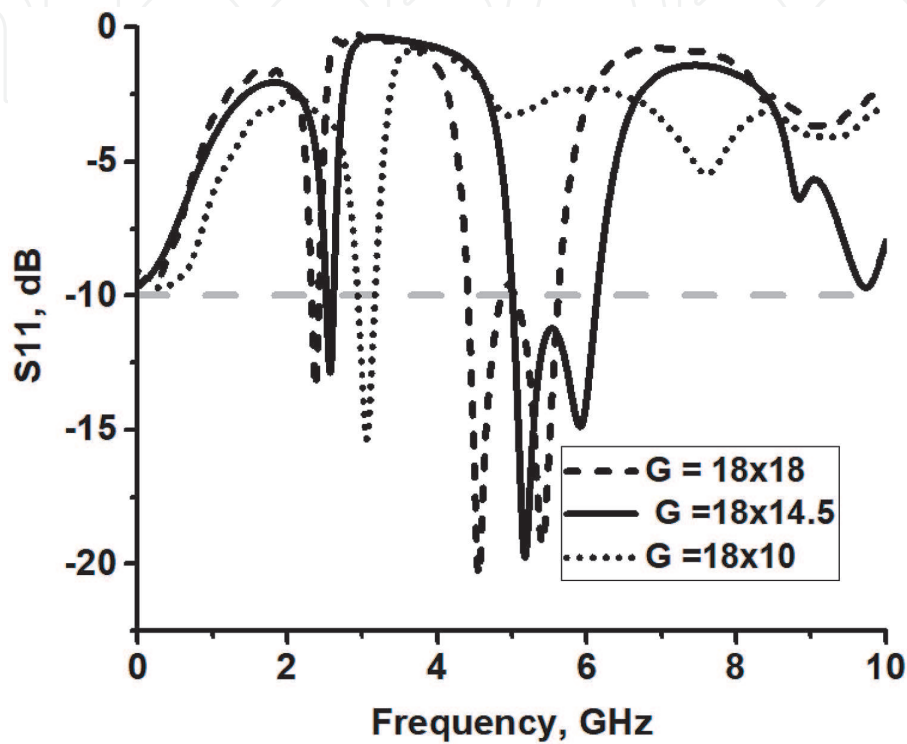


Figure 7.
The effect of ground plate size on reflection coefficient.

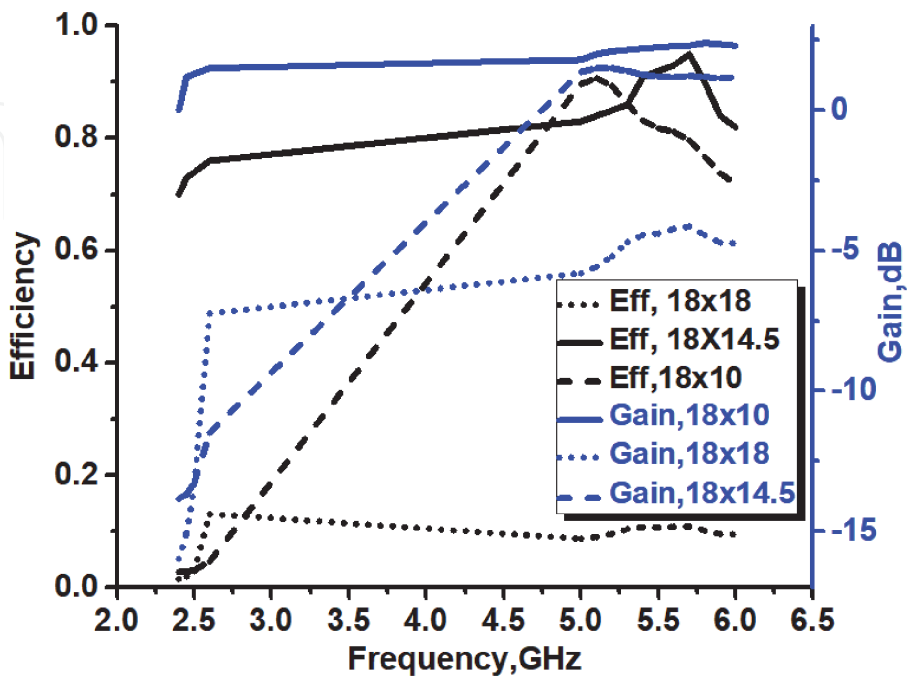


Figure 8.
The effect of ground plate size on the gain and the radiation efficiency [17].

Iteration	1st BW (2.4–2.6)	2nd BW (5–6)	Efficiency %	ARBW (GHz)	Gain (dB)	State
0th	(4–4.5)	(8.1–9.4)	40	—	–12 to 0	The resonant frequencies are out of the required, LP
1st	(3.1–3.6)	—	40–55	0.1	–8 to 0	2nd band disappeared, ARBW around 3.4 GHz
2nd	(2.6–2.7)	(5.4–6.4)	50–60	0.07	–2 to 1	Does not cover all required frequencies, ARBW around 5 GHz
3rd	(2.5–2.6)	(5–6)	55–68	0.2	–1.5 to 1.6	Does not cover all frequencies at the 1st band, ARBW around 3.5 GHz
4th	(2.4–2.6)	(4.9–6)	65–85	0.1, 0.3	0–2.4	Optimum

Table 2.
The radiation properties for all iterations of the dual-input fractal antenna.

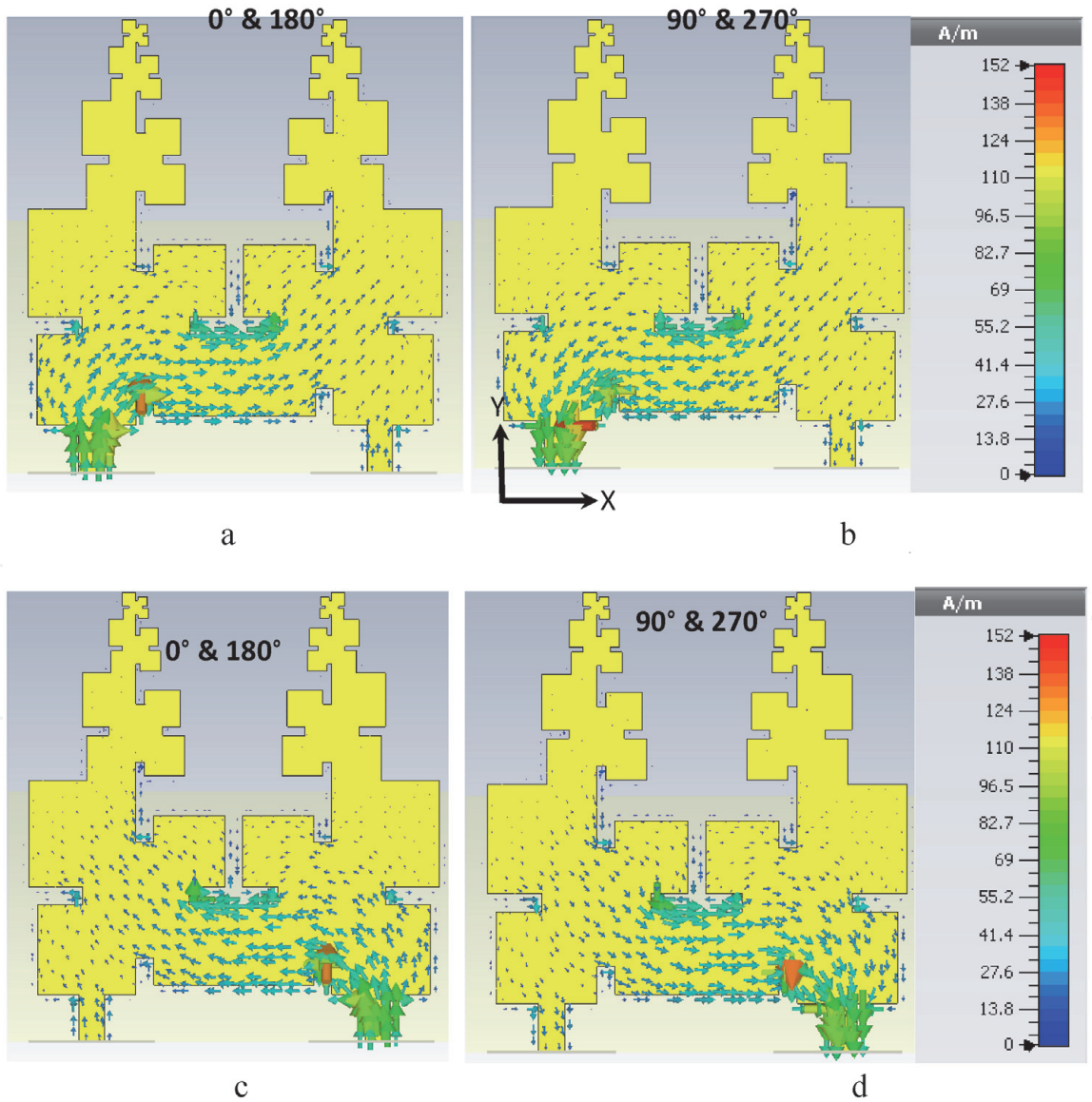


Figure 9.
Surface currents at 2.45 GHz for both inputs. (a) First input at 0° and 180° phase references. (b) First input at 90° and 270° phase references. (c) Second input at 0° and 180° phase references. (d) Second input at 90° and 270° phase references [17].

indicated by the dotted curve in **Figure 7**. The dashed curve in **Figure 7** represents the value of return losses when the dimensions of the ground plate are 18 mm × 18 mm, the lower band shifts to 2.3 GHz, while the upper band covers the 4.4–5.6 GHz frequency range. These bands are not suitable for Wi-Fi, WiMAX, and ISM applications. The solid curve in **Figure 7** indicates that the ground plate has optimum dimensions of 18 mm × 14.5 mm and that the dual notched bands meet the purpose of designing the fractal antenna.

Figure 8 presents the effect of ground size on the radiation efficiency (black curves) and gain (blue curves) of the proposed antenna. As shown in **Figure 8**, a fully grounded antenna (18 mm × 18 mm) has a low radiation efficiency (blue dotted curve) and gain (black dotted curve), especially at the lower operating band. The values of simulated gain and radiation efficiency are improved by reducing the size of the ground plate to 18 mm × 10 mm as indicated by the dashed curves in **Figure 8**. The gain increases to 0–1.5 dB at the lower operating band and to 1.5–2.5 dB at the upper operating band. Meanwhile, the radiation efficiency increases to 70–90% when the ground size is set to 18 mm × 14.5 mm as indicated by the black solid curve in **Figure 8**. Therefore, the optimum dimensions of the ground are 18 mm × 14.5 mm.

Table 2 illustrates some important radiation properties for each iteration, such as impedance bandwidth, efficiency, gain, and ARBW.

2.3 Surface current and circular polarization

Figure 9 shows the simulated surface current at the resonant frequency of 2.45 GHz for phase references of 0°, 90°, 180°, and 270°. When the first input for phase references at 0° and 180° is excited, most of the surface current direction on the feed strip line is along the +Y before circulating counter clockwise, as shown in **Figure 9a**.

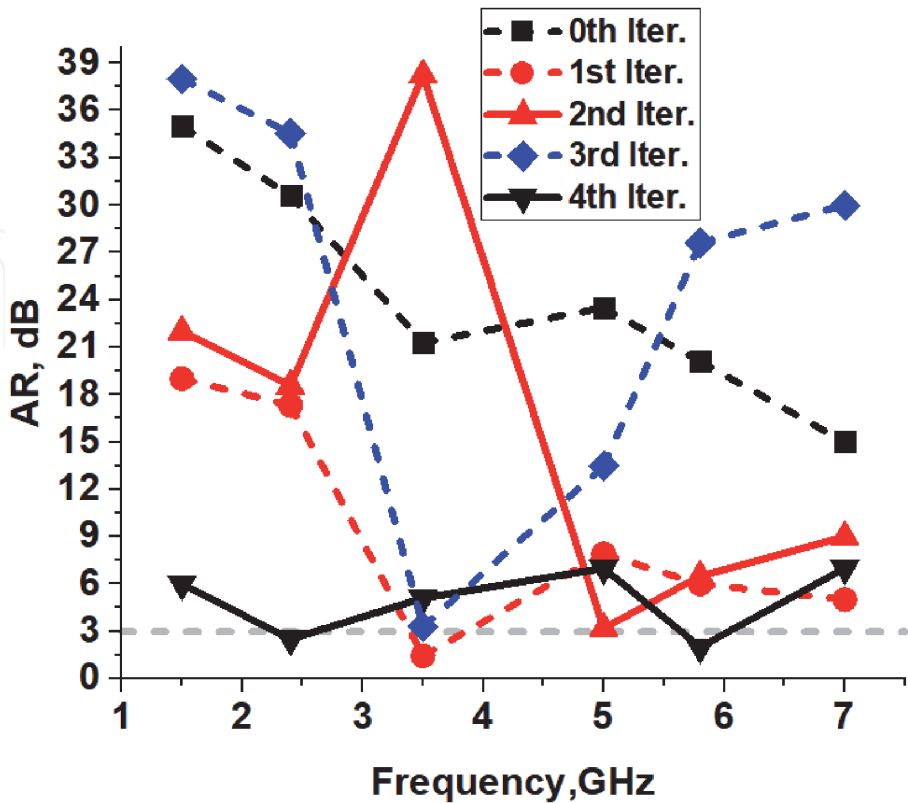


Figure 10.
Simulated axial ratio for all iterations [17].

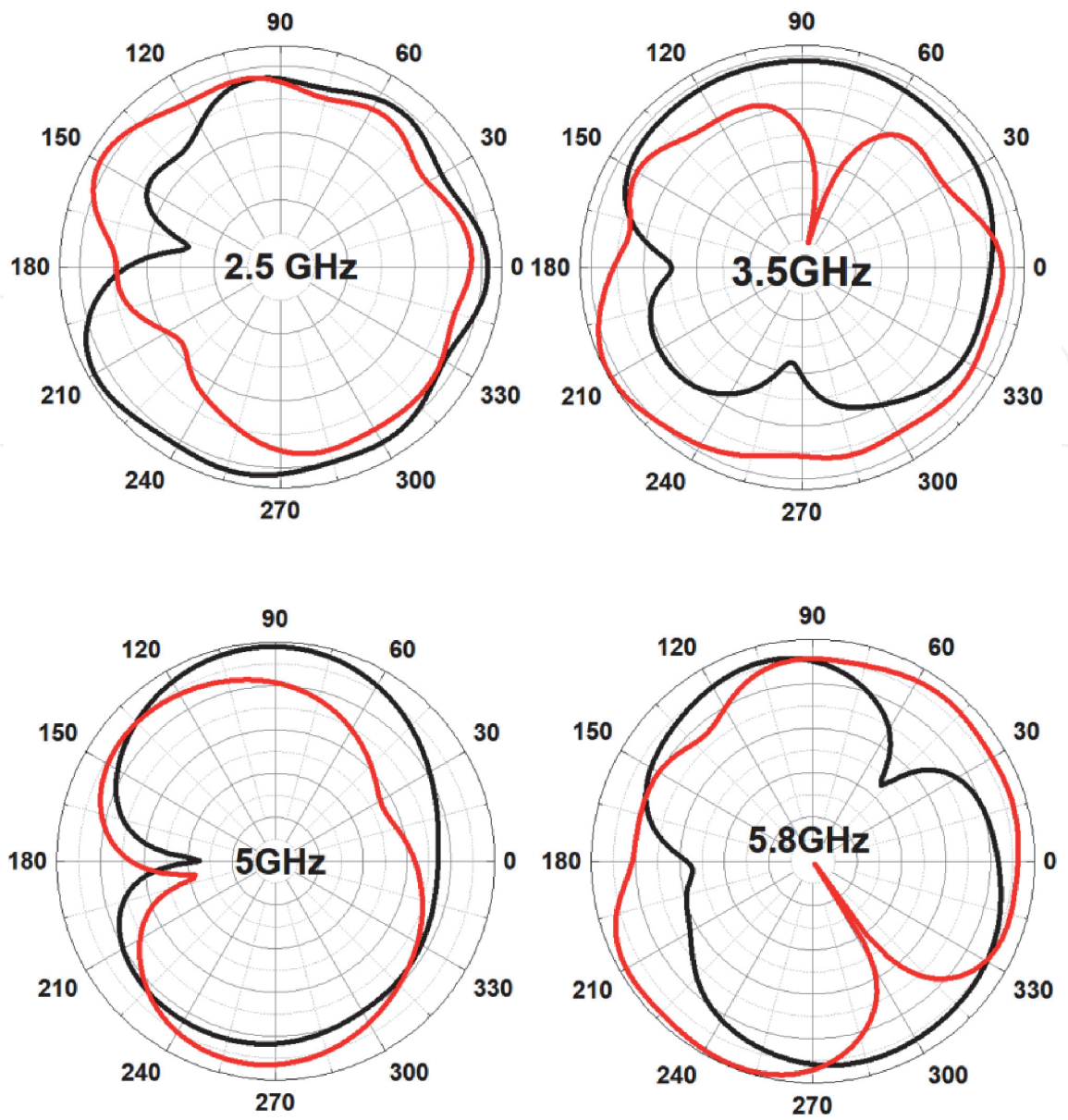


Figure 11.
Left (black curves) and right (red curves) polarization at 2.5, 3.5, 5, and 5.8 GHz [17].

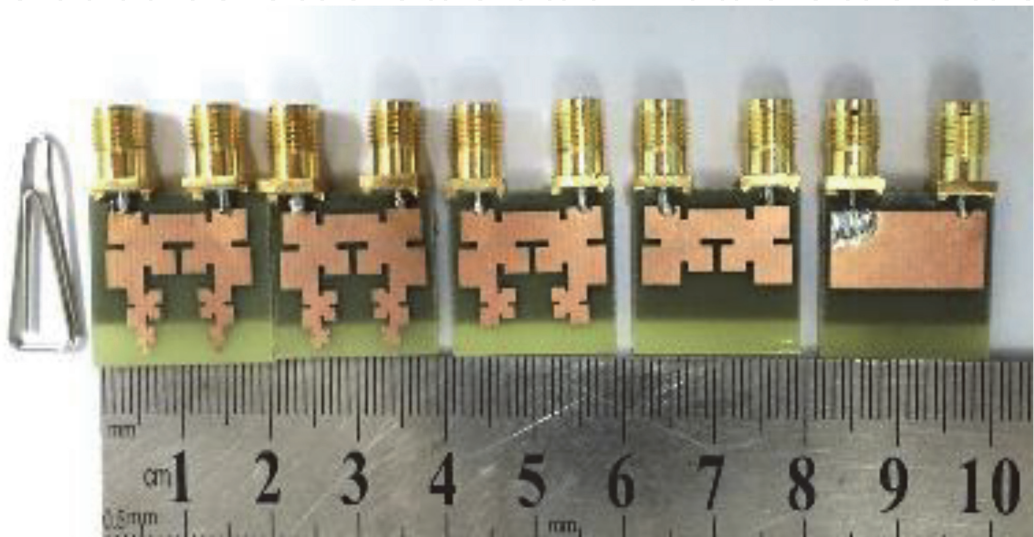


Figure 12.
The prototypes for all iterations [17].

For phase references at 90° and 270° , the surface current flows towards the $-Y$ direction along the strip feeding line and then circulates clockwise, as shown in **Figure 9b**. Contrary to that, when the second input is excited, the surface current direction on the feed strip line and the circulating direction of the current changed, as shown in **Figure 9c** and **d**. RHCP and LHCP can be achieved by switching the two inputs. The signals of LHCP and RHCP can be received simultaneously. Thus, the proposed antenna has a dual circular polarization.

Figure 10 presents the AR values for all iterations. The AR values at the 0th iteration are too high, especially at the lower operating band as indicated by the dashed black curve. These values have changed during the configuration of the proposed antenna as shown in **Figure 10**. The ARBW of 0.09 GHz, which is approximately 66% of that of the lower operating band, is indicated by the solid black curve. Meanwhile, the ARBW of 0.35 GHz is approximately 30% of that of the upper operating band. The ARBW values in **Figure 10** match those that have been reported in previous circular polarization studies as shown in **Figure 10**.

Figure 11 shows the left and right polarizations at the frequencies of 2.5, 3.5, 5, and 5.8 GHz. The phase differences between the radiation patterns at 3.5 GHz and 5 GHz are 170° and 15° , respectively, whereas the LHCP and RHCP patterns at 2.5 GHz and 5.8 GHz shift by 88° (almost perpendicular to each other). Therefore, the antenna demonstrates circular polarization around the frequencies of 2.5 and 5.8 GHz. The antenna structure has zigzag edges that are configured by the arrangement of modified patches and creates lengthy paths for the surface current. At some frequencies, such as 2.5 and 5.8 GHz, the components of the surface currents are perpendicular to each other, thereby exciting orthogonal electric fields that, in turn, result in circular polarization [18]. The AR values in **Figure 10** and the current distribution in **Figure 9** match each other. The circular polarization is improved by the special design and arrangements of the modified structure during the antenna configuration, and the orthogonal components are generated at the resonant frequencies of 2.5 and 5.8 GHz.

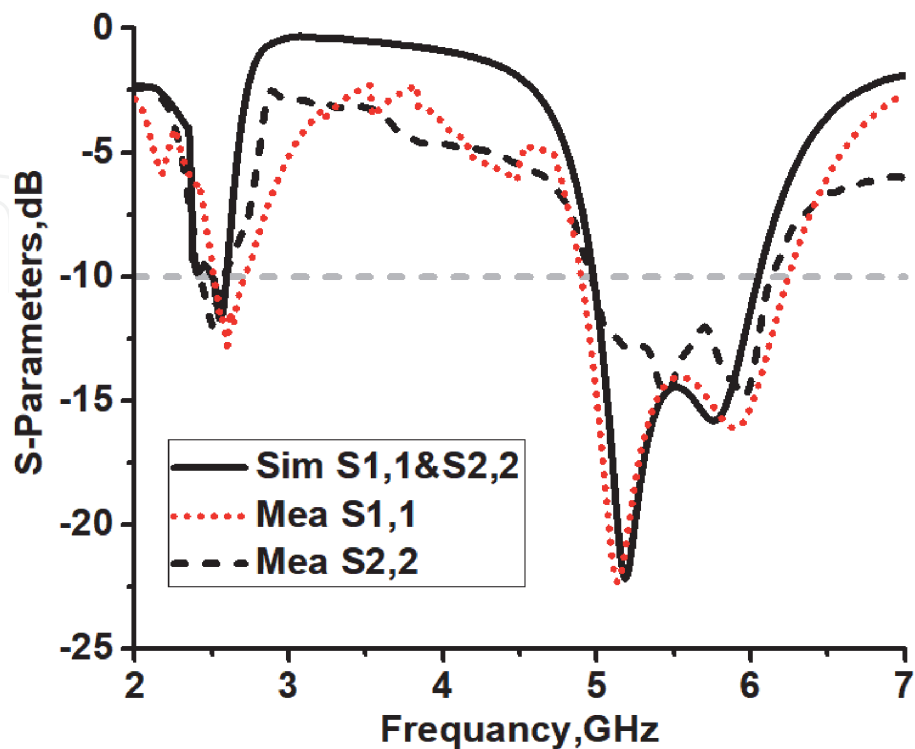


Figure 13.
The simulated and measured *S*-parameters for the proposed antenna [17].

2.4 Measurements and results

The five iterations are fabricated as shown in **Figure 12**. The compact size of the proposed fractal antenna is clear in this figure. The physical dimensions of the 0th iteration are the same of that for the fourth iteration, while the electrical length of the fourth iteration is much greater than the 0th iteration.

Figure 13 illustrates the simulated and measured reflection coefficients of the proposed fractal antenna. Generally, good matching is observed between simulated data (the solid curve) and the measured data (dashed and red dotted curves). However, several resonant frequencies in the experimental results are shifted unlike those in the simulated curve. Shifting occurs due to the impurity of materials used

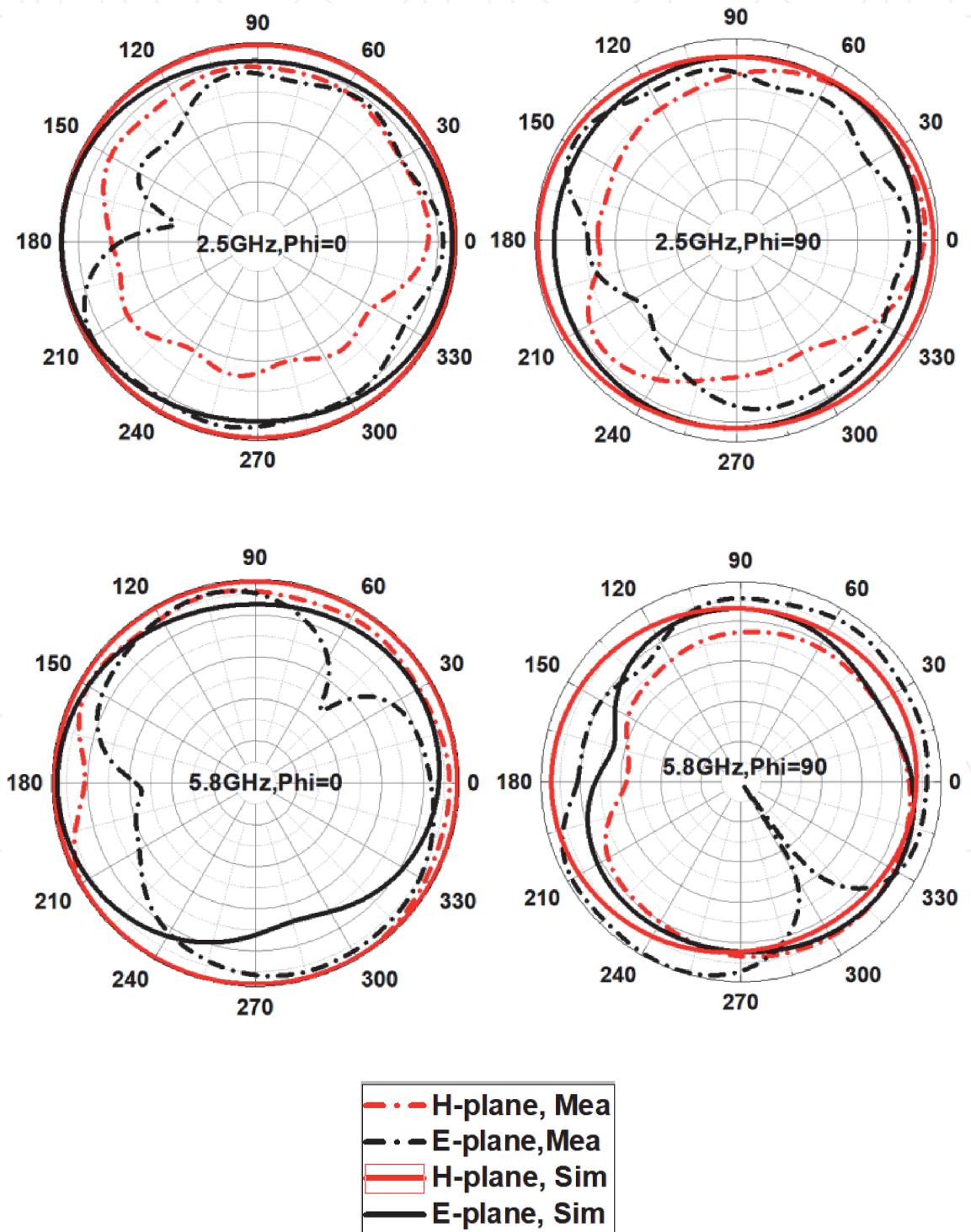


Figure 14.
Simulated and measured radiation patterns in E&H planes [17].

in the prototype. The impedance bandwidth of the first input (the red dotted curve) expanded to the range of 2.4–2.63 GHz and 4.8–6.4 GHz.

The measured reflection coefficient for the second input S_{22} is represented in **Figure 13** by the dashed curve. The measured impedance bandwidth expanded to the frequency band of 2.38–2.6 GHz and 4.9–6.1 GHz with low values of the reflection coefficient. Since the antenna is not MIMO antenna, the mutual coupling between the dual inputs S_{12} and S_{21} is not important in these measurements.

Figure 14 presents the simulated and measured radiation patterns on the E and H planes. The red or black solid curves represent the simulated data, while the red or black dashed curves represent the experimental results. The measured and simulated radiation curves in **Figure 14** show an acceptable agreement.

The measured radiation patterns on the H plane (the red dashed curve) at all resonant frequencies are almost omnidirectional. The E and H planes measured at 2.5 and 5.8 GHz when $\phi = 90$ are perpendicular to each other, which matches the CP characteristics and the results of previous theoretical works on CP generation as shown in **Figures 11** and **12**. Meanwhile, the radiation pattern at the lower resonant frequency of 2.5 GHz is almost omnidirectional because the length of the surface current path is approximately half the wavelength of this frequency. Therefore, no side lobes are observed in its radiation pattern. As the frequency increases, the surface current path becomes greater than the wavelength of this frequency, thereby producing many side lobes at their radiation patterns. The radiation pattern is almost omnidirectional at resonant frequencies lower than 2.5 GHz because the length of the surface current path is approximately half the wavelength of this frequency. Therefore, side lobes are not observed in its radiation pattern. As the frequency increases, the surface current path becomes greater than the wavelength of this frequency, causing many side lobes at their radiation patterns.

The proposed fractal antenna displays an ARBW of 2.48–2.55 and 5.6–5.9 GHz, which is lesser than 3 dB as shown in **Figure 15** (the blue squared points) which is about 35% of the first operating band 2.4–2.6 GHz and about 30% of the second band 5–6 GHz. The values of the measured gain (the black circular points) vary

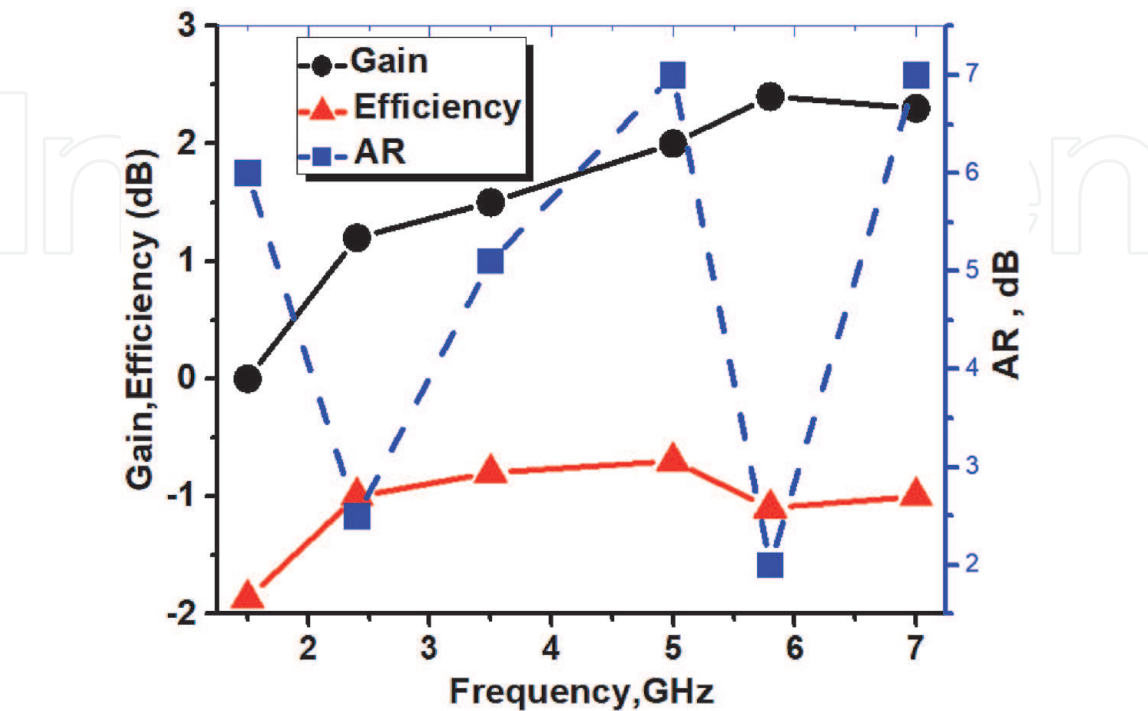


Figure 15.
The measured gain, efficiency, and AR [17].

between 0 dB at 2.5 GHz and 2.7 dB at 5.8 GHz. Meanwhile, the maximum efficiency (the red triangle points) is -0.7 dB (85%) at 5 GHz.

3. Meandered ring fractal antenna

The universal serial bus (USB) dongles are used in many portable communication devices such as laptops and pads in order to transmit and receive the data with a high bit rate. Since USB dongles are used with portable devices, the desired antenna must solve serious challenges such as the size, multiband, and the stability of radiation characteristics during the notched bands (gain and efficiency).

The aim of this study is to design a fractal ring antenna with a compact size and low profile, configured by three iterations, which covered the frequency range that meets the specification of the upper operating band for Wi-Fi and WIMAX applications and has high efficiency and stable radiation properties.

3.1 Antenna design

In this study, the proposed antenna with a compact size of $24 \times 9 \times 0.8$ mm³ was configured by a three-step process. The radiator of reference antenna (**Figure 16**) is a square patch with dimensions $x = y = 9$ mm and is separated from the ground by a gap of 0.3 mm. According to empirical Eq. (7), the dimension of the square patch will be equal to 36 mm for the resonant frequency ($f_r = 5$ GHz) and substrate FR-4 with $\epsilon_r = 4.3$. To miniaturize the dimension of the antenna, let $X = Y = \frac{1}{4} \times 36$ mm = 9 mm. The ground plate features a rectangular shape with dimensions of 9.7×9 mm². The radiator and ground are printed on the same side of commercial substrate (FR-4) with $\epsilon_r = 4.3$, $\tan \delta = 0.027$, and thickness = 0.8 mm. **Figure 16** shows the first iteration in the design of antenna with square slot cuts in the radiator plate to configure the square ring with arm width equal to $0.1x$. In the second iteration, the square ring is modified as a meandered ring to increase its electrical length to generate more resonant frequencies, which are collected to obtain a notched operating band of 4.4–6.7 GHz which is shown in **Figure 16** (the solid curve). All dimensions of the meandered ring are denoted as a function of x , which corresponds to the dimension of the square ring in the first iteration, as indicated in **Figure 16**. The length of the square ring in the first iteration equals $4x$.

$$\text{Length of the upper arm} = 0.5X + 0.3X + 0.1X + 0.12X + 0.34X = 1.36X \quad (13)$$

$$\text{Length of left arm} = 0.34X + 0.17X + 0.1X + 0.22X + 0.38X = 1.21X \quad (14)$$

$$\text{Length of bottom arm} = 0.4X + 0.13X + 0.1X + 0.17X + 0.47X = 1.27X \quad (15)$$

$$\text{Length of right arm} = 0.44X + 0.1X + 0.1X + 0.13X + 0.52X = 1.29X \quad (16)$$

Thus, the total length of meandered ring equals $5.13X$. The length of meandered ring increases by a factor of 1.28 compared with the length of the square ring of the same size in the first iteration. Of course, the increase in length of the four arms leads to increase in the length of the surface current paths and thus generates new resonant frequencies which collected together to give a wide impedance bandwidth, and this is clear in **Figure 17** (the solid curve) where the operating band increased when the ring becomes meandered at the second iteration.

Figure 17 depicts the real (black curves) and imaginary (blue curves) parts of the impedance values for the three antennas. The values of real-part impedance

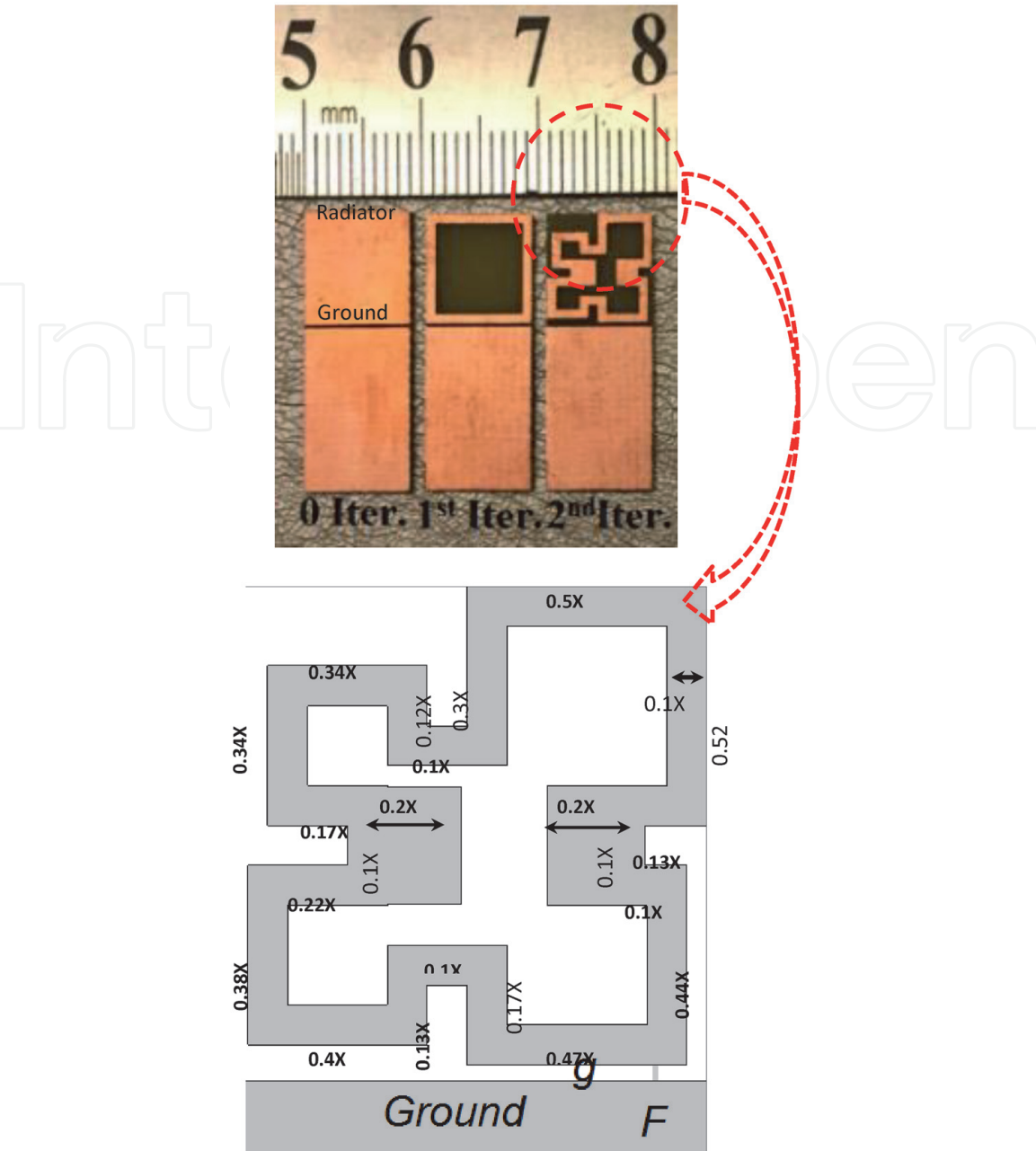


Figure 16.
The process of configuring the meandered ring antenna [19].

for all antennas are almost equal at frequencies < 4.7 GHz. Thereafter, the values of real-part impedance for the second iteration are closer to the input impedance of excitation port (50 ohms red line), especially in the frequency range of 5.1–6.4 GHz.

Figure 18 shows that negative imaginary values (capacitance) are observed in the curves of imaginary part impedance for all antennas at frequencies < 4.4 GHz. In the frequency band of 4.4–6 GHz, the values of the imaginary part are closer to zero (red line), that is, only real-part impedances for the three antennas are resistant. This property provides stable matching factor that leads to stable gain and efficiency in the operating band.

Table 3 illustrates some important radiation properties for each iteration, such as impedance bandwidth, efficiency, gain, and ARBW. It is clear that most of the required specifications that can be achieved at the second iteration are due to improving the values of radiation properties during the progress of antenna configuration, especially the impedance bandwidth, efficiency, gain, and an ARBW as shown in **Table 3**.

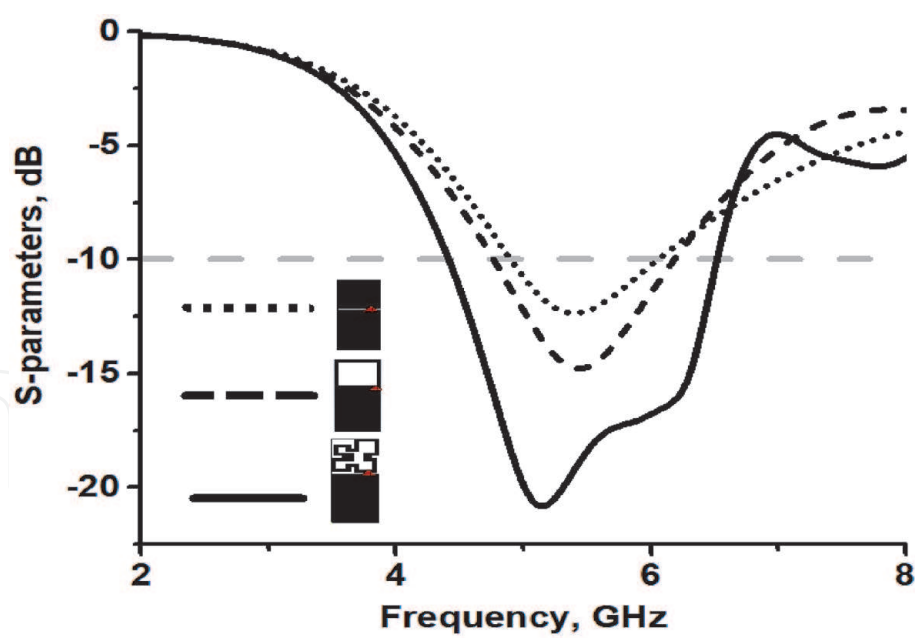


Figure 17.
The simulated reflection coefficient for the 0th iteration, first iteration, and the second iteration [19].

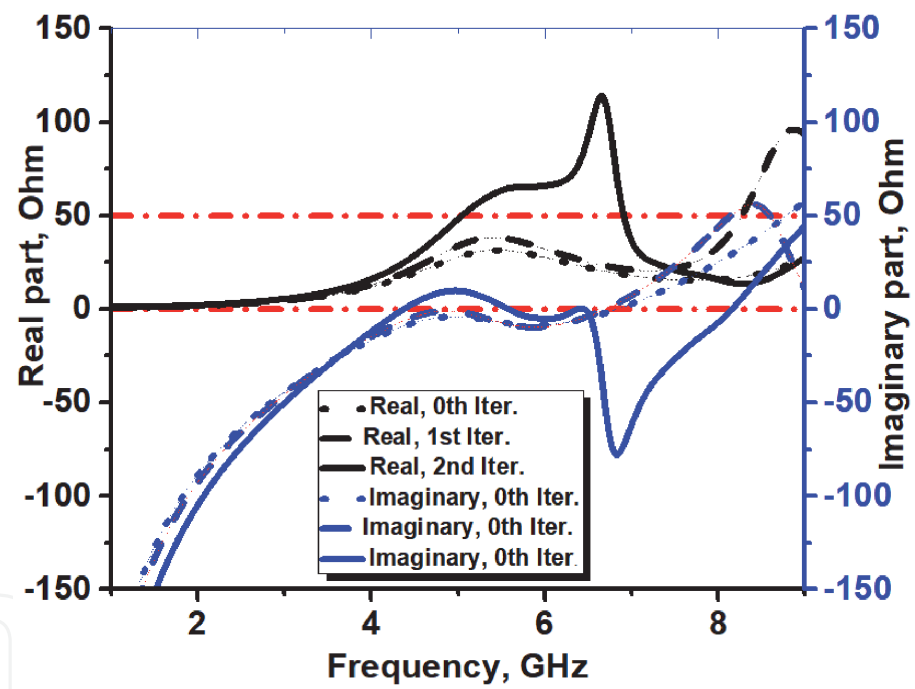


Figure 18.
The impedance values of the three iterations [19].

Iteration	BW (GHz)	Efficiency (%)	ARBW (GHz)	Gain (dB)	Lower S1, 1 (dB)	State
0th	(5.2–6)	50–65	—	–12 to 0	–10	Low efficiency, low gain, and LP
1st	(4.7–6)	60–75	—	1–3	–14	Does not have stable value of gain, LP
2nd	(4.4–6.7)	85–90	0.083	2.2–2.4	–20	Optimum

Table 3.
The radiation properties for all iterations of the meandered ring fractal antenna.

3.2 Current distribution

The maximum distribution currents at 5 GHz for the 0th iteration are mainly concentrated close to the feeding point on the patch and ground plates, as shown in **Figure 19**. In the first iteration, the currents are distributed in the additional area, especially on the square ring, which leads to the generation of new resonant frequency. The operating band is expanded compared with that at 0th iteration. The distribution of the surface current on ground plate is the same in all iterations because there is no change in surface current path at the ground plate during the progress of antenna configuration compared with the radiator plane.

Figure 19 (second iteration) shows that the surface current has two paths. The first path begins from the feeding point F and then passes through the right arm to point A, which has a total length equal to $1.79X = 16$ mm, which is approximately one-fourth of the wavelength for the resonant frequency at 5 GHz.

The total length of the other path, which is almost perpendicular to the first and begins from feeding point F and then passes through the bottom arm to point B, is equal to $1.87X = 17$ mm, which is approximately one-fourth of the wavelength for the resonant frequency at 5 GHz. Thus, two equal components of surface current normal to each other provide circular polarization radiation at 5 GHz.

3.3 Circular polarization

The length of the first surface current path from feeding point F to point A is 16 mm, which is almost equal to the length of the second surface current path from the feeding point to point B. These normal components are approximately $\frac{1}{4}$ of the wavelength for 5 GHz generated CP, as shown in **Figure 20**, which represents surface current distributions for phases at 0° , 90° , 180° , and 270° at 5 GHz resonant frequency. Surface current circulates clockwise along the upper and lower right quarters and counterclockwise along the lower left quarter for 0° and 180° phases. **Figure 20** shows the circulation direction of surface current when the phase becomes 90° and 270° .

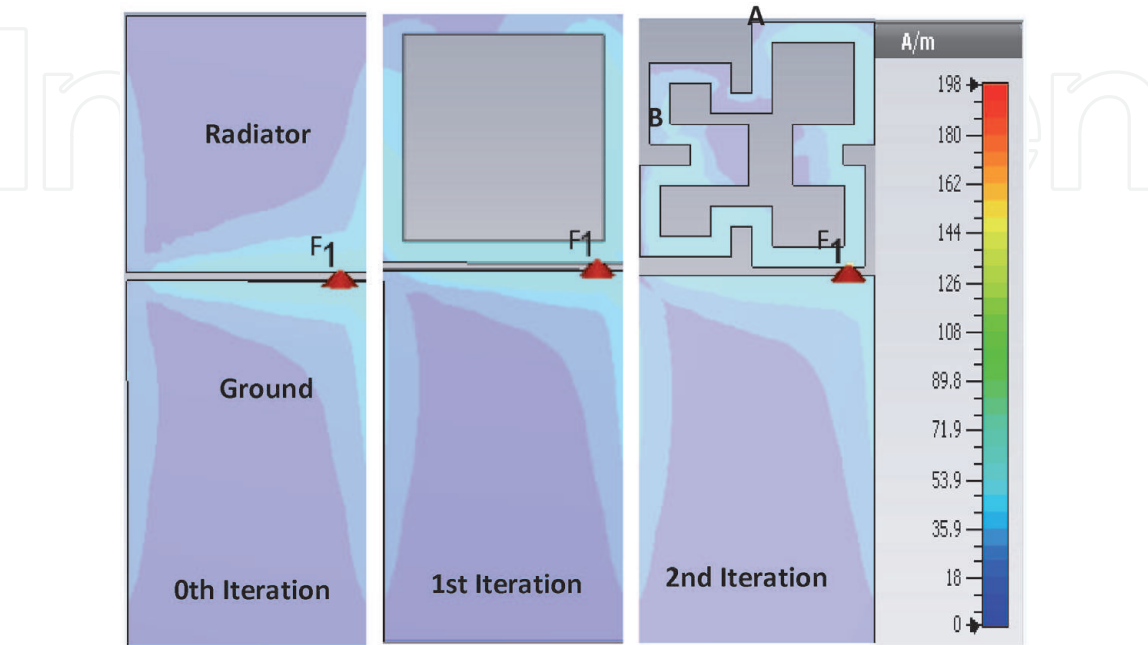


Figure 19.
The surface current at 5 GHz for all iterations [19].

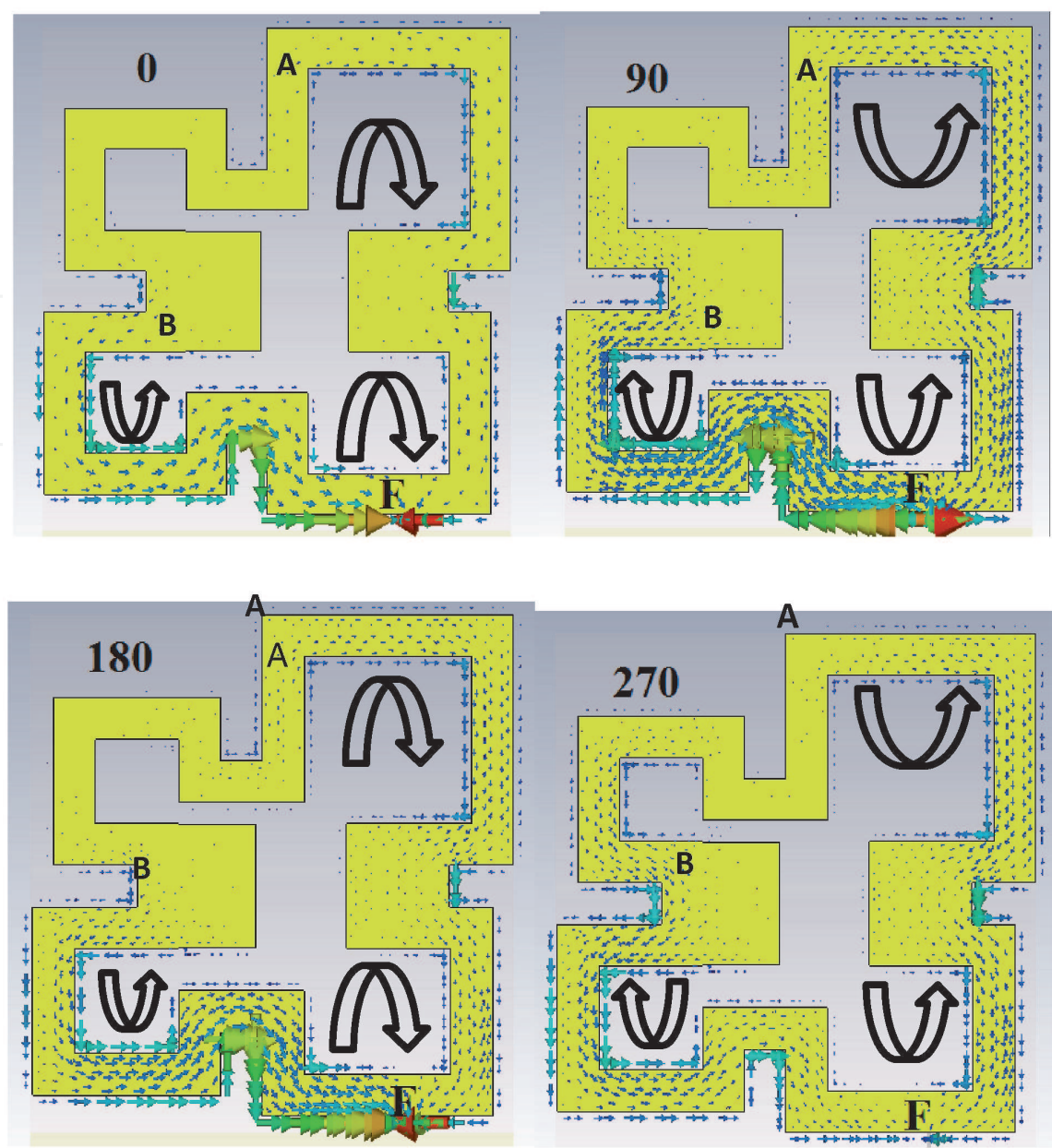


Figure 20. Surface current for sequential phases (0° , 90° , 180° , and 270°) at 5 GHz [19].

Figure 21 depicts the left and right polarizing radiation in E-plane at 5 and 5.8 GHz, which show that the phase differences at 5 and 5.8 GHz is approximately 86° and 180° , thereby indicating that CP is radiated at 5 GHz only. This study matches the surface current distribution, which indicates that a circular polarization radiation at 5 GHz is generated by dual orthogonal components of electrical field created by the surface currents that flow along the perpendicular arms of the meandered ring at the feed point, as shown in **Figure 20**.

3.4 Measurements and results

Figure 22 represents the photographs of the all iteration prototypes; it is clear that the size of the proposed antenna is compact that can be used for portable communication devices.

The measured impedance bandwidth for the proposed antenna compresses to the frequency band of 4.8–6.7 GHz compared with the simulated impedance

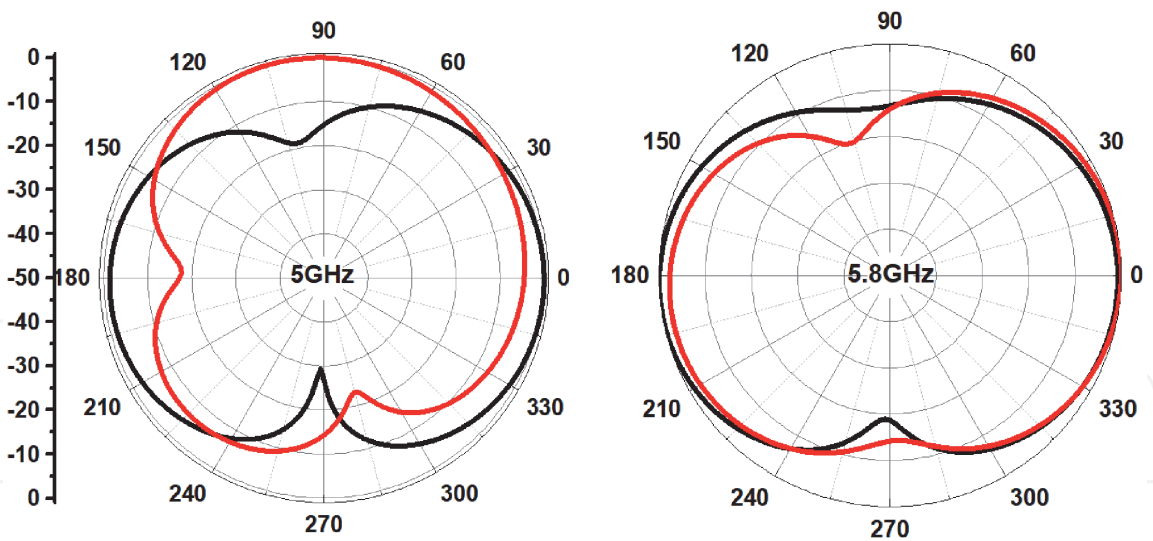


Figure 21.
Simulated left (black curves) and right (red curves) polarization in E-plane at 5 and 5.8 GHz [19].

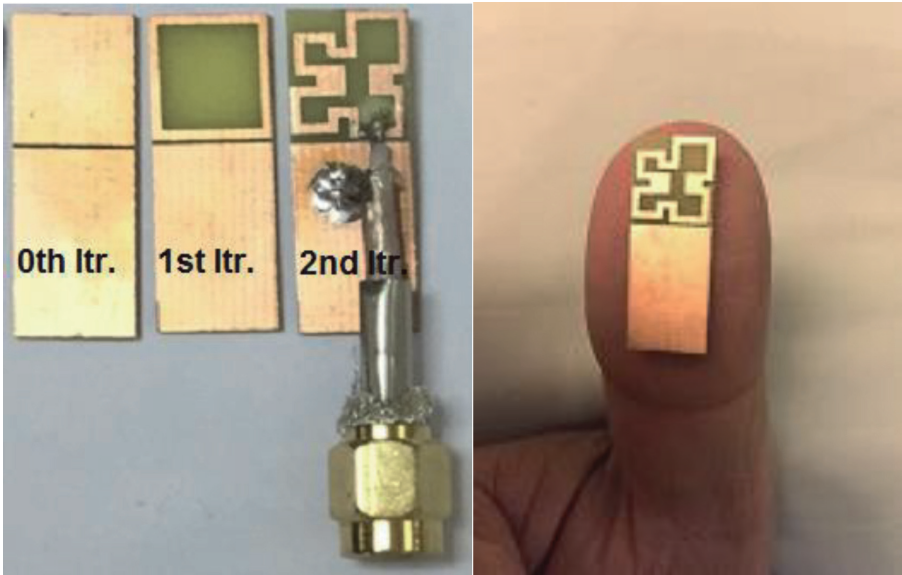


Figure 22.
The prototypes of all fractal antenna iterations [19].

bandwidth of 4.4–6.7 GHz, and the resonant frequency shifted to 5 GHz compared with 5.8 GHz for the simulated value as shown in **Figure 23**. That takes place due to impurities of some of the materials that are used in prototypes and due to the soldering.

Figure 24 shows a distinguishing agreement between simulated (solid) and measured (dashed) patterns. Radiation patterns in the H-plane (black curves) for the proposed antenna are almost omnidirectional at 5 and 5.8 GHz. **Figure 24b** shows that the radiation pattern at 5.8 GHz is similar to that at 5 GHz, but the former is more directional. At E-plane (when $\phi = 0$), the radiation patterns looked like number 8 where two major lobes observed shifted by an angle of 180° as shown in **Figure 24a** (the red curves), while at 5.8 GHz, the radiation pattern in E-plane had dual asymmetrical major lobes.

Figure 25 depicts the measured values of the gain, efficiency, and an axial ratio. At frequency bands of 5–6 GHz, gain values are almost constant 2.3–2.4 dB, and efficiency reaches -0.45 dB (90%), whereas axial ratio bandwidth measures 83

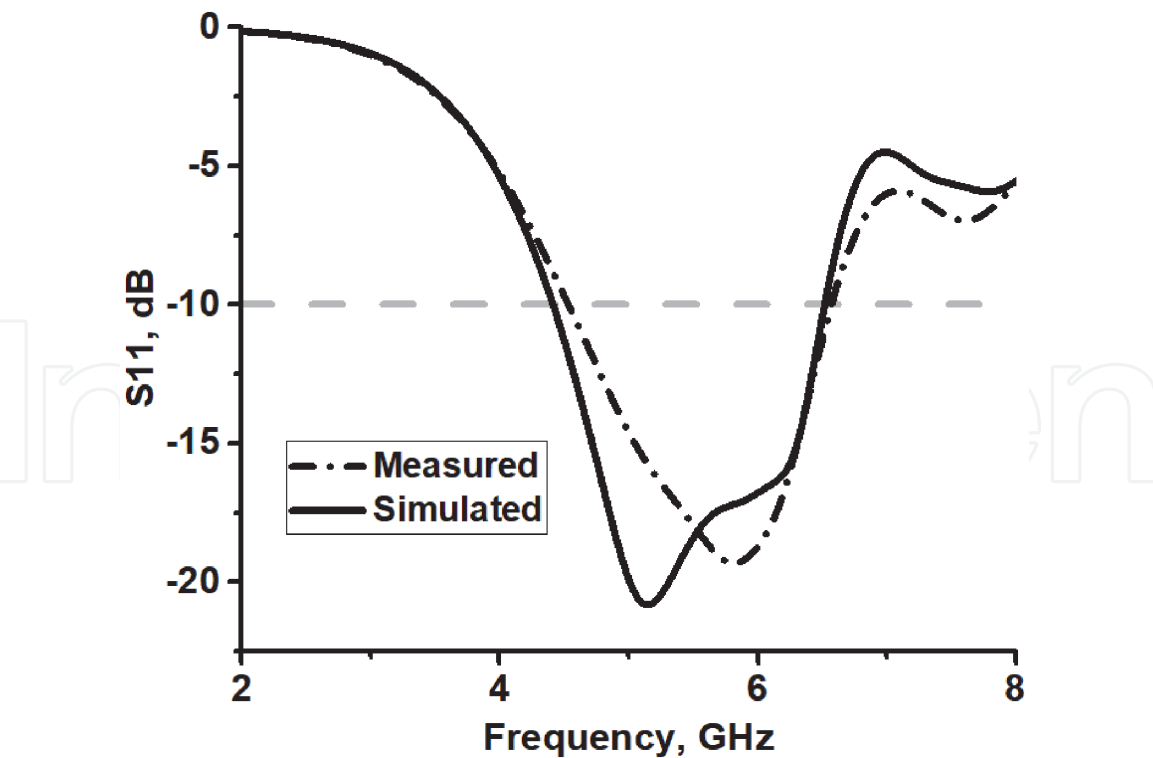


Figure 23.
Measured (dashed) and simulated (solid) $S_{1,1}$ for the proposed antenna [19].

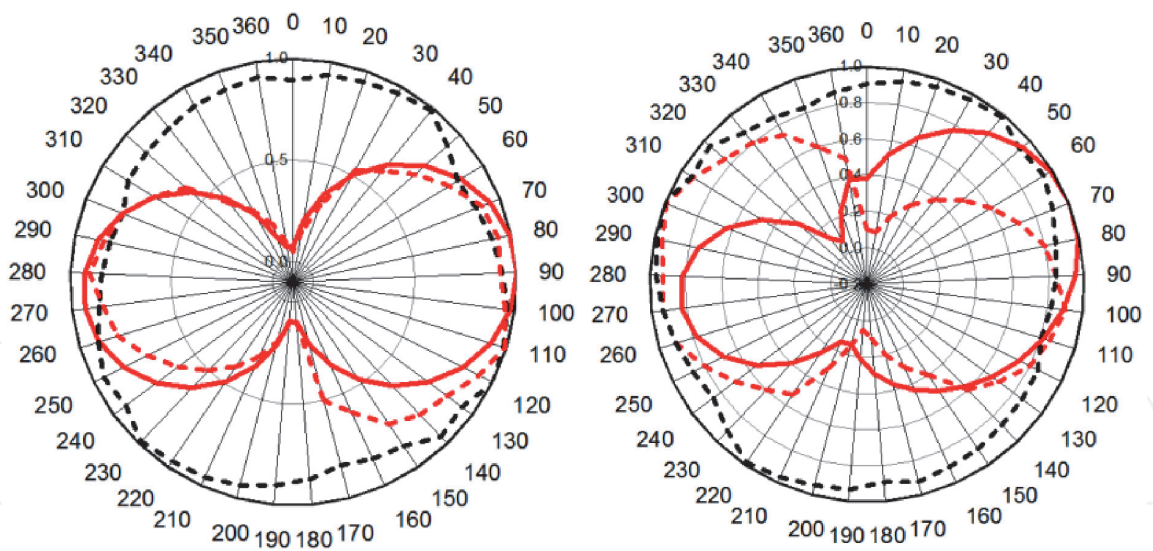


Figure 24.
Simulated (solid) and measured (dashed) radiation pattern. (a) At 5 GHz. (b) At 5.8 GHz [19].

MHz (approximately 8.3% of operating band) around a resonant frequency of 5 GHz.

Although the meandered ring fractal antenna has impedance bandwidth that covers only the upper band required for Wi-Fi, WiMAX, and ISM applications, it has stable radiation properties especially the gain and the efficiency. Furthermore, the meandered ring antenna has high efficiency (90%), highly compact size, and omnidirectional radiation pattern in H-plane that can be used for portable Wi-Fi and WiMAX devices.

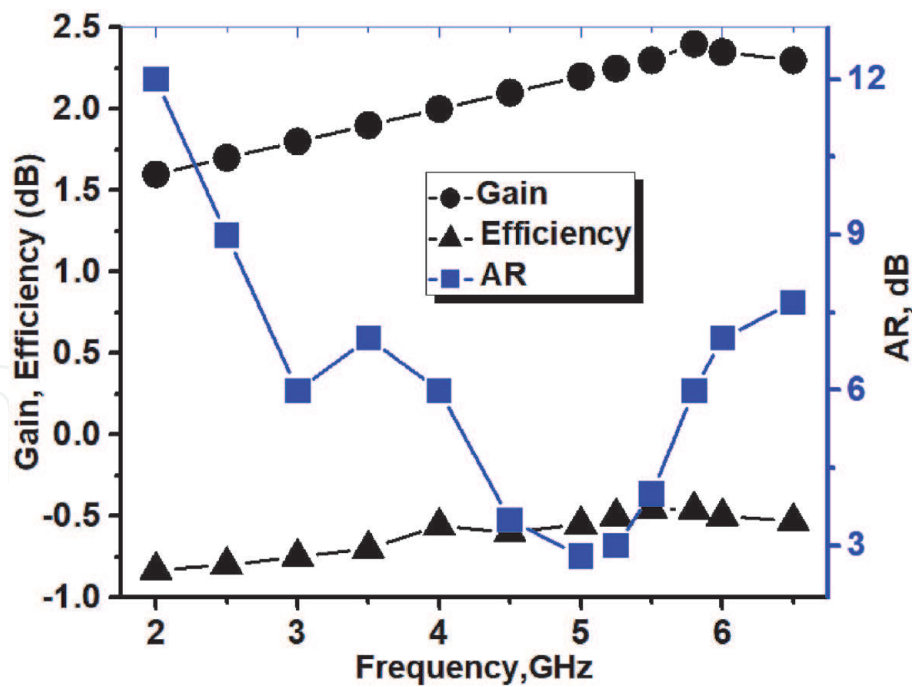


Figure 25.
Measured gain, efficiency, and AR for the antenna [19].

4. Conclusion

Fractal geometry is another type of micro strip antenna used in designing antennas. Two fractal antennas, namely, dual-input fractal antenna and meandered ring antenna, were investigated. All antennas are fabricated on commercial and cheap FR-4 substrate. The proposed fractal antennas are CP radiated by generating orthogonal components of electrical field.

The prototype of the dual-input fractal antenna has a compact size, which is approximately 9 and 16% of the Q-slot [20] and crescent slot [21] antenna size, respectively. The measured operating bands for the first input of the fractal antenna are 2.38–2.62 GHz and 5–6 GHz, whereas those for the second input of the fractal antenna are 2.4–2.65 and 4.8–6.2 GHz. The prototype of the dual-input fractal antenna displays an ARBW of 2.48–2.55 and 5.6–5.9 GHz, which is approximately 35% of the first operating band 2.4–2.6 GHz and approximately 30% of the second band 5–6 GHz. The values of the measured gain vary between 0 dBi at 2.5 GHz and 2.7 dBi at 5.8 GHz. The maximum efficiency is –0.7 dB (85%) at 5 GHz.

The fourth investigated antenna in this study is the meandered ring fractal antenna with compact size, which is approximately 9% of that of the Q-slot antenna, 10% of the crescent slot antenna size, and 66% of dual-input fractal antenna size. However, the meandered ring antenna only covers the upper bandwidth of 5–6 GHz used for Wi-Fi and WiMAX applications. The proposed antenna in this study has a small size, low profile, high measured efficiency (90%), stable gain (2.3–2.4) dBi, and CP radiation with an ARBW of 0.083 GHz, which is approximately 6% of the measured operating band at 4.8–6.2 GHz. Thus, the meandered ring monopole antenna is suitable for the requirements of portable communication devices.

Table 4 shows that the previous fractal antennas have circular polarization radiation, such as those reported in [3], which is the Giuseppe Peano fractal antenna that covered the frequency band of 1.5–4 GHz and ARBW of 0.2 GHz,

Ant.	BW (GHz)	Gain (dB)	ARBW (GHz)	Size (mm)	Effie. (%)	Weak points
[3]	(1.5–2.7)	3–4	0.2	60 × 60 × 10	40–80	Does not cover all required bands, low efficiency at lower frequency, used air gap
[6]	(2.32–2.52) (3.37–3.45) (5.6–5.9)	0.5 to –6	0.06, 0.09, 0.3	50 × 50 × 3.2	—	Used RT/duroid substrate, does not cover all frequencies in the upper band
[23]	(2.7–10.3)	—	1.1	54 × 36 × 1.5	85–95	No values of gain, missed 2.5 GHz band
[24]	(3.4–3.6)	6	0.1	40 × 40 × 1	91	Missed 2.4 GHz and 5 GHz bands
[22]	(2.2–2.6)	1.8t–4.6	0.6	100 × 100 × 13	—	Covered only 2.4 GHz band, large, no efficiency values
Fractal antenna	(2.4–2.6) (4.7–6.5)	0–2.4	0.07, 0.3	18 × 18 × 0.8	70–85	Missed 3.5 GHz band
Meander ring	(4.8–6.2)	2.3–2.4	0.083	24 × 9 × 0.8	85–90	Missed 2.4 GHz and 3.5 GHz bands

Table 4.
Comparisons between proposed fractal antennas and previous related works.

and the fractal antenna proposed in [6] whose size is approximately twice as that of the proposed fractal antenna is used in this study. The antenna has an ARBW of 0.06, 0.09, and 0.3 GHz at the three operating bands, but it does not cover all of the required frequencies, especially at the band of 5–6 GHz.

The meandered line fractal antenna is CP with an ARBW of 0.6 GHz reported in [22]. This meandered line antenna only covered the first band. The size of this antenna is very large and its efficiency has not been mentioned in the report. Modified Koch curve is used in designing the antenna based on Fibonacci sequence reported by [23]. The antenna is miniaturised to 54 × 36 × 1.5 mm and covered the frequency band (2.7–10.3) GHz with an ARBW of approximately 1.1 GHz around resonant frequency 6 GHz. The antenna does not cover the lower band (2.4–2.6) GHz, its CP radiation around 6 GHz, uses unbalanced feeding coaxial, and no gain values.

Therefore, the two proposed fractal antennas in the current study (dual fractal and meandered ring antennas) have specific characteristics better than the previous related antennas in **Table 4**. They are the best when possibly applied for Wi-Fi, WiMAX, and ISM communication purposes for the following reasons:

Firstly, the dual-input fractal antenna has dual operating bands for Wi-Fi (IEEE 802.11b,g,n) and WiMAX (IEEE 802.16e), Wi-Fi (IEEE802.11y), Wi-Fi (IEEE 802.11a,h,j,n), and WiMAX (IEEE 802.16d). The meandered ring fractal only covers the upper band (5–6) GHz.

Secondly, acceptable and greater values of gain for both antennas than the specified gain for fractal antennas in **Table 4** compared with their compact size.

Thirdly, the two types of fractal antennas are highly efficient (>80%), which matched the specific efficiency in **Table 4**. Despite the small size of the proposed antennas compared with many of the previous fractal antennas in **Table 4**, the manufactured antennas in the present study are characterized by superior and stable efficiency, thereby making them suitable for Wi-Fi and WiMAX applications.

Fourthly, the circular radiation properties at some operating bands for both proposed fractal antennas, that overcome the limits of generation CP with wide

ARBW in a compact size, especially the dual fractal antenna, which has CP radiation during the first and third bands, can avoid many serious problems, such as mismatched polarization and multipath interferences.

Fifthly, the highly compact size and omnidirectional radiation patterns in H-plane, especially the meandered ring antenna, facilitated the possibility of using the proposed antennas for mobile Wi-Fi and WiMAX communication devices.

Sixthly, aside from being low profile and easy to fabricate and the use of commercial FR-4 substrate in addition to existing features, these antennas can be adopted for the purpose for which they are designed.

Author details

Amer T. Abed^{1*}, Mahmood J. Abu-AlShaer² and Aqeel M. Jawad²

1 Communication Engineering Department, Al-Mamun University College, Baghdad, Iraq

2 Al-Rafidain University College, Filastin, Baghdad, Iraq

*Address all correspondence to: amer.t.abed@ieee.org

IntechOpen

© 2020 The Author(s). Licensee IntechOpen. This chapter is distributed under the terms of the Creative Commons Attribution License (<http://creativecommons.org/licenses/by/3.0>), which permits unrestricted use, distribution, and reproduction in any medium, provided the original work is properly cited. 

References

- [1] Werner DH, Gangul S. An overview of fractal antenna engineering research. *IEEE Antennas and Propagation Magazine*. 2003;**45**:38-57
- [2] Chen W-L, Wang G-M, Zhang C-X. Bandwidth enhancement of a microstrip-line-fed printed wide-slot antenna with a fractal-shaped slot. *IEEE Transactions on Antennas and Propagation*. 2009;**57**:2176-2179
- [3] Oraizi H, Hedayati S. Miniaturization of microstrip antennas by the novel application of the Giuseppe Peano fractal geometries. *IEEE Transactions on Antennas and Propagation*. 2012;**60**: 3559-3567
- [4] Chaimool S, Chokchai C, Akkaraekthalin P. Multiband loaded fractal loop monopole antenna for USB dongle applications. *Electronics Letters*. 2012;**48**:1446-1447
- [5] Srivatsun G, Subha Rani S. Compact multiband planar fractal cantor antenna for wireless applications: An approach. *International Journal of Antennas and Propagation*. 2012;**2012**
- [6] Reddy V, Sarma N. Triband circularly polarized Koch fractal boundary microstrip antenna. *IEEE Antennas and Wireless Propagation Letters*. 2014;**13**:1057-1060
- [7] Tripathi S, Mohan A, Yadav S. Hexagonal fractal ultra-wideband antenna using Koch geometry with bandwidth enhancement. *IET Microwaves, Antennas & Propagation*. 2014;**8**:1445-1450
- [8] Weng W-C, Hung C-L. An H-fractal antenna for multiband applications. *IEEE Antennas and Wireless Propagation Letters*. 2014;**13**:1705-1708
- [9] Dhar S, Patra K, Ghatak R, Gupta B, Poddar DR. A dielectric resonator-loaded minkowski fractal-shaped slot loop heptaband antenna. *IEEE Transactions on Antennas and Propagation*. 2015;**63**:1521-1529
- [10] Li D, Mao J-F. Coplanar waveguide-fed Koch-like sided Sierpinski hexagonal carpet multifractal monopole antenna. *IET Microwaves, Antennas & Propagation*. 2014;**8**:358-366
- [11] Yogesh Kumar Choukiker SKB. Wideband frequency reconfigurable Koch snowflake fractal antenna. *IET Microwaves, Antennas & Propagation*. 2017;**11**:203-208
- [12] Abed AT, Singh MS, Islam MT. Amer fractal slot antenna with quad operating bands high efficiency for wireless communications. In: 2016 IEEE 3rd International Symposium on Telecommunication Technologies (ISTT). 2016. pp. 6-8
- [13] Abed AT. Novel sunflower MIMO fractal antenna with low mutual coupling and dual wide operating bands. *International Journal of Microwave and Wireless Technologies*. 2020
- [14] Abed AT. A new fractal antenna flame structure with impedance ration 10.6: 1 high efficiency for UWB applications. *Al-Ma'mon College Journal*. 2017:215-231
- [15] Abed AT. A novel coplanar antenna butterfly structure for portable communication devices, a compact antenna with multioperating bands. *IEEE Antenna and Propagation Magazine*. 2020
- [16] Werner DH, Haupt RL, Werner PL. Fractal antenna engineering: The theory and design of fractal antenna arrays. *IEEE Antennas and Propagation Magazine*. 1999;**41**:37-58
- [17] Amer MSJS, Abed T, Islam MT. Compact fractal antenna circularly

polarised radiation for Wi-Fi and WiMAX communications. IET Microwaves, Antennas & Propagation. 2018;**12**:2218-2224

[18] Abed AT, Singh MSJ, Jawad AM. Investigation of circular polarization technique in Q-slot antenna. International Journal of Microwave and Wireless Technologies. 2020;**12**:176-182

[19] Abed AT, Singh MS, Islam MT. Compact-size fractal antenna with stable radiation properties for Wi-Fi and WiMAX communications. KSII Transactions on Internet & Information Systems. 2018;**12**

[20] Abed A, Singh M. Slot antenna single layer fed by step impedance strip line for Wi-Fi and Wi-Max applications. Electronics Letters. 2016;**52**:1196-1198

[21] Abed AT, Singh MSJ, Islam MT, Khaleel AD. Dual crescent-shaped slot antenna fed by circular polarisation into dual orthogonal strip lines. IET Microwaves, Antennas & Propagation. 2017;**11**:2129-2133

[22] Luo K, Chen B, Ding W-P. Meander line coupled cavity-backed slot antenna for broadband circular polarization. IEEE Antennas and Wireless Propagation Letters. 2015;**14**:1215-1218

[23] Chetna Sharma SM, Vishwakarma DK. Miniaturization of spiral antenna based on fibonacci sequence using modified Koch curve. IEEE Antennas and Wireless Propagation Letters. 2017;**16**:932-935

[24] Cai T, Wang G-M, Zhang X-F, Shi J-P. Low-profile compact circularly-polarized antenna based on fractal metasurface and fractal resonator. IEEE Antennas and Wireless Propagation Letters. 2015;**14**:1072-1076